NASA TECHNICAL NOTE

NASA TN D-2872

NASA TN D-2872

GPO PRICE $ _____

CFSTI ~~OTS~~ PRICE(S) $ 3.00

Hard copy (HC) _____

Microfiche (MF) .75

FACILITY FORM 602

N65-26413 (ACCESSION NUMBER) | (THRU)

63 (PAGES) | 1 (CODE)

(NASA CR OR TMX OR AD NUMBER) | 30 (CATEGORY)

EFFECT ON METEOR FLIGHT OF COOLING BY RADIATION AND ABLATION

by H. Julian Allen, Barrett S. Baldwin, Jr., and Nataline A. James

Ames Research Center
Moffett Field, Calif.

NATIONAL AERONAUTICS AND SPACE ADMINISTRATION • WASHINGTON, D. C. • JUNE 1965

NASA TN D-2872

EFFECT ON METEOR FLIGHT OF COOLING BY RADIATION AND ABLATION

By H. Julian Allen, Barrett S. Baldwin, Jr.,
and Nataline A. James

Ames Research Center
Moffett Field, Calif.

NATIONAL AERONAUTICS AND SPACE ADMINISTRATION

For sale by the Clearinghouse for Federal Scientific and Technical Information
Springfield, Virginia 22151 – Price $3.00

EFFECT ON METEOR FLIGHT OF COOLING BY RADIATION AND ABLATION

By H. Julian Allen, Barrett S. Baldwin, Jr.,
and Nataline A. James
Ames Research Center

SUMMARY

26413

The parameters of meteor flight are evaluated taking account of surface radiation as well as vapor ablation. Results are presented for four meteoroid materials: tektite, stone, pumice, and iron. The calculations are based on a spherical shape with a range in radii of 10^{-8} to 5×10^{-3} meters. Entry velocities from 11 to 70 kilometers per second are considered. Because of an approximate similarity a large range of entry angles is covered. The validity of this approximation and of a number of assumptions is investigated. A significant result of the investigation is the rediscovery of surface radiation as a possible explanation, instead of fragmentation, for the anomalous behavior of the light curves of faint meteors.

Author

INTRODUCTION

It is usual in meteor physics to assume (e.g., see refs. 1 and 2) that the heat energy resulting from the collision of air molecules with the surface of a meteoroid is completely accounted for by vapor ablation of the surface. This assumption is a reasonable one for meteoroids of centimeter size and larger. Whipple (ref. 3) showed that if the size of the body at atmosphere entry is sufficiently small, say of the order of a micron or less, then the reradiation of heat from the meteoroid alone will suffice to keep the surface cool enough that essentially no ablation will occur. It is the purpose of this paper to analyze the motion and heating of meteoroids of sizes between the two extremes in order to answer, for a wide range of speeds, such questions as: (1) At what size does melting occur and over what range of altitudes does the molten state exist? (2) Under what conditions will a nonrotating body with a molten front face have a solid rear face? (3) What is the maximum size for which one may expect free molecular flow to exist? (4) Up to what size will a molten drop remain essentially spherical? (5) When will the dynamic pressure overbalance the surface tension and break up a molten drop? (6) For what meteoroid materials will vapor ejected from the front face significantly alter the drag force? (7) How does the size of the meteorite vary with the initial size of the meteoroid, and, in particular, for irons, is the calculated meteorite size-abundance relation in agreement with that obtained from cosmic dust collections from polar ice caps? (8) At what altitude does the speed fall to a trivially low value? and finally, (9) What is the behavior of the luminosity of these bodies with respect to both maximum magnitude, and magnitude variation with altitude?

In the analysis four meteoroid materials have been considered. In addition to the usual stone and iron, we have included tektite, which Chapman (ref. 4) has indicated to be of lunar origin, and a low density material with the character of pumice. Much of the needed information on radiative and vaporization properties of meteoroid materials is contained in reference 5. The important physical characteristics assumed for these materials are listed in table I. The symbols in the analysis are those used in meteor theory and familiar to astrophysicists; the system of units is the meter-kilogram-second.

SYMBOLS

The quantities used in the analysis along with the units in which they are expressed are the following:

a	meteoroid frontal area at any time t, corresponding to altitude h, m^2
$\bar{a}$	dimensionless meteoroid frontal area, a/a_∞
a_∞	meteoroid frontal area at atmosphere entry, m^2
b	sticking coefficient
c_1, c_2	constants in the vapor pressure-temperature equation
d	diameter of vapor molecule, assumed to be 2×10^{-10} m
h	instantaneous altitude, m
I	luminous intensity, τ_0 kg m^3 sec^{-4}
I_{max}	maximum luminous intensity, τ_0 kg m^3 sec^{-4}
i	luminous intensity coefficient, sec^{-1}
i_{max}	maximum luminous intensity coefficient, sec^{-1}
Kn	Knudsen number, l/r
k	thermal conductivity of the meteoroid, W m^{-1} $^{\circ}K^{-1}$
L	Avogadro's number, 6.02252×10^{23} $mole^{-1}$
l	mean free path of air at altitude h, m
M	molecular weight of meteor vapor, kg $mole^{-1}$
m	meteoroid mass at time t, corresponding to altitude h, kg
$\bar{m}$	dimensionless meteoroid mass, m/m_∞

m_∞ meteoroid mass at atmosphere entry, kg

m_{v_1} vapor mass from front face of meteoroid, kg

n_1 number of vapor molecules from the front surface of the meteoroid flowing through the stream tube of area a

p_v meteoroid saturation vapor pressure at temperature T, N m^{-2}

p_{v_1} front surface meteoroid vapor pressure at temperature T_1, N m^{-2}

p_{v_2} rear surface meteoroid vapor pressure at temperature T_2, N m^{-2}

q heat input in kinetic energy units, J

R gas constant (8.3143/M), m^2 sec^{-2} $^oK^{-1}$

r meteoroid radius at any time t, corresponding to altitude h, m

$\bar{r}$ dimensionless radius, r/r_∞

r_o final (meteorite) radius at sea level, m

r_∞ meteoroid radius at atmosphere entry, m

s surface area of the meteoroid at any time t, m^2

T temperature, ^oK

T_f melting temperature of meteoroid, ^oK

T_1 front surface temperature, ^oK

T_2 rear surface temperature, ^oK

t time, sec

V meteoroid velocity at any time t, corresponding to altitude h, m sec^{-1}

$\bar{V}$ dimensionless meteoroid velocity, V/V_∞

V_∞ meteoroid velocity at atmosphere entry, m sec^{-1}

We Weber number, $\rho V^2 r/\tau_s$

x distance measured ahead of the body in the direction of motion, m

Z_R zenith angle (trajectory angle measured from vertical), rad

β inverse of over-all scale height for density, m^{-1}

β' inverse of local scale height for density, m^{-1}

γ drag coefficient

γ_v coefficient of the drag increment due to meteoroid vaporization

ϵ radiation emissivity (assumed to be 0.92)

ζ energy required to vaporize a unit mass of the meteoroid, $m^2\ sec^{-2}$ ($J\ kg^{-1}$)

η kinetic to ablation energy ratio, $\lambda V\epsilon^2/12\gamma\zeta$

λ heat-transfer coefficient

ξ dimensionless air density factor

ρ air density at altitude h, $kg\ m^{-3}$

$\bar{\rho}$ dimensionless air density, ρ/ρ_o

ρ_m meteoroid density, $kg\ m^{-3}$

ρ_o sea-level air density, 1.225 $kg\ m^{-3}$

ρ_{v_1} front surface meteor saturation vapor density, $kg\ m^{-3}$

σ Stefan-Boltzmann constant, $5.6697\times10^{-8}\ W\ m^{-2}\ {}^{o}K^{-4}$

τ_o luminous efficiency factor, $I\ sec^4\ kg^{-1}\ m^{-3}$

τ_s liquid meteoroid surface tension, $N\ m^{-1}$

ψ molecular screening factor (ratio of total area of vapor molecules in the stream tube ahead of the meteoroid to the meteoroid frontal area)

ω mass evaporation rate per unit area, $kg\ m^{-2}\ sec^{-1}$

ω_1 front surface evaporation rate per unit area, $kg\ m^{-2}\ sec^{-1}$

ω_2 rear surface evaporation rate per unit area, $kg\ m^{-2}\ sec^{-1}$

ASSUMPTIONS

(1) The weight can be ignored and the earth assumed flat in the motion calculation.

(2) For the motion and ablation calculations, the meteoroid is initially a nonrotating sphere before entering the atmosphere and it remains a nonrotating sphere as it ablates.

(3) The flow is free molecular. The limits for which this assumption is applicable are examined.

(4) Change in the heat stored within the body can be ignored compared with the heat removed by radiation and by ablation of the surface as vapor.

(5) A temperature difference between the front and rear surfaces of the body may exist. For purposes of calculation of this effect, the body is treated as a slab of thickness equal to the radius.

(6) The variation of atmospheric density and mean free path with altitude is given by the 1959 U. S. Standard Atmosphere (ref. 6).

Most of these assumptions are usual in meteor theory. The justifications for them have been so fully discussed in the literature that no additional remarks are felt to be needed here.

ANALYSIS

Since, for the most part, the analytical development herein is that of the classical theory of meteors (see, e.g., ref. 5), derivations of formulas, in the main, are included only where they are new or obscure in the literature.

In accordance with the first assumption the meteor flight path is a straight line, so that time can be expressed in terms of altitude through

$$dt = -\frac{dh}{V \cos Z_R} \tag{1}$$

The equation of motion for the meteoroid is, with assumption (1),

$$m \frac{dV}{dt} = -\gamma \rho V^2 a \tag{2}$$

With assumption (2) and equation (1) this becomes

$$\frac{d\overline{V}}{dh} = \frac{3\rho_o \gamma}{4\rho_m r_\infty \cos Z_R} \left(\frac{\overline{\rho}\overline{V}}{\overline{r}}\right) \tag{3}$$

The heat input rate is given by

$$\frac{dq}{dt} = \frac{1}{2} \lambda \rho V^3 a \tag{4}$$

In accordance with assumption (4) the heat balance gives

$$\frac{\lambda \rho V^3 a}{2} = \frac{1}{2} \epsilon \sigma s (T_1{}^4 + T_2{}^4) + \frac{1}{2} \zeta s (\omega_1 + \omega_2) \tag{5}$$

With assumption (2) this becomes

$$\frac{2\rho_0 V_\infty^3}{4}(\bar{\rho}\bar{V}^3) = \epsilon\sigma(T_1^4 + T_2^4) + \zeta(\omega_1 + \omega_2) \tag{6}$$

The heat received by the rear face must be conducted from the front face so that in accordance with assumption (5)

$$\frac{k}{r}(T_1 - T_2) = \frac{k}{r_\infty}\left(\frac{T_1 - T_2}{\bar{r}}\right) = \epsilon\sigma T_2^4 + \zeta\omega_2 \tag{7}$$

The mass loss by ablation is

$$\frac{dm}{dt} = -V \cos Z_R \frac{dm}{dh} = -\frac{1}{2}s(\omega_1 + \omega_2) \tag{8}$$

With assumption (2) this becomes

$$\bar{V}\frac{d\bar{r}}{dh} = \frac{\omega_1 + \omega_2}{2\rho_m V_\infty r_\infty \cos Z_R} \tag{9}$$

To use equations (6), (7), and (8) it is necessary to express the evaporation rate in terms of the surface temperature. For a Maxwellian distribution of efflux velocities (see ref. 5, p. 24)

$$\omega_1 = \frac{bp_{v_1}}{\sqrt{2\pi RT_1}} = \frac{b\times 10^{c_1+(c_2/T_1)}}{\sqrt{2\pi RT_1}} \tag{10a}$$

and

$$\omega_2 = \frac{bp_{v_2}}{\sqrt{2\pi RT_2}} = \frac{b\times 10^{c_1+(c_2/T_2)}}{\sqrt{2\pi RT_2}} \tag{10b}$$

The quantity b is the so-called sticking coefficient (see ref. 7, p. 65 and ref. 8). For iron b is near 1.0. For solid stone b can be small, but according to reference 8, its value should be near 1.0 for liquid stone. Since evaporation of stone from the solid state is not appreciable we shall set $b = 1.0$ throughout the present investigation.

To use equations (3) and (5) we must also provide the heat transfer and drag coefficients. With assumption (3) and complete accommodation of molecular impact of the air on the surface

$$\lambda = 1 \tag{11}$$

The drag coefficient would also be unity for complete accommodation but when the vaporization of the front surface differs from that of the rear surface, then a drag increment due to vaporization will be present in the amount

$$\gamma_v \rho V^2 a = \frac{1}{2}a(p_{v_1} - p_{v_2}) \tag{12}$$

or

$$\gamma_V = \frac{1}{2\rho_o V_\infty^2}\left[\frac{10^{c_1+(c_2/T_1)} - 10^{c_1+(c_2/T_2)}}{\bar{\rho}\bar{V}^2}\right] \tag{13}$$

and the total drag coefficient will thus be

$$\gamma = 1 + \gamma_V \tag{14}$$

Using the foregoing equations one can calculate the entry characteristics for a meteoroid in free molecular flow. For a nonablating body, the free molecular flow limit occurs when the body size at any altitude becomes comparable with the mean free path of the air molecules at that altitude. In other words the Knudsen number

$$Kn = \frac{l}{r} \tag{15}$$

must be substantially larger than unity (say, about 5).

The free molecular flow limit for an ablating body may also be due to ablating vapor molecules colliding with a sufficient fraction of the air molecules ahead of the body, thus, effectively shielding the body from these air collisions. The screening factor, which is a measure of the departure from free molecular flow, may be found as follows: The vapor density at the front surface of the body is

$$\rho_{V_1} = \frac{p_{V_1}}{RT_1} = \frac{10^{c_1+(c_2/T_1)}}{RT_1} \tag{16}$$

and at any time the total mass of vapor in the stream tube of unit area ahead of the body is

$$\frac{m_{V_1}}{a} = \int_{x=r}^{\infty} \rho_{V_1}\left(\frac{r}{x}\right)^2 dx = \rho_{V_1} r \tag{17}$$

The number of vapor molecules per unit area is then

$$\frac{n_1}{a} = \frac{Lm_{V_1}}{a} = L\rho_{V_1} r = \frac{Lr10^{c_1+(c_2/T_1)}}{RT_1} \tag{18}$$

The diameter of each molecule is d, so that the total cross section of all vapor molecules in the stream tube of unit area is

$$\psi = \pi d^2\left(\frac{n_1}{a}\right) = \frac{\pi d^2 L r_\infty}{R}\left[\frac{\bar{r}10^{c_1+(c_2/T_1)}}{T_1}\right] \tag{19}$$

If the free molecular flow assumptions are to apply, the screening factor, ψ, should be small compared to unity (say, 0.1 or less). However, it may well be that even for much larger values, the departure of the heat transfer and the drag coefficient from free molecular flow values may not be great. In the results presented later there are plots showing the values of entry parameters that lead to maximum values of $\psi \cos Z_R$ equal to 0.1, 0.3, 0.5, and 1.0. A similar criterion for screening due to vapor molecules is given in reference 7 on pages 35-39 and 82-85.

A second limitation (see ref. 5) which applies to the analysis is that the meteoroid should stay essentially spherical during entry and must remain intact. When the dynamic pressure, ρV^2, becomes comparable with the internal pressure in the molten drop due to surface tension, the body becomes distorted from a spherical shape. Further increase of dynamic pressure flattens the drop, and when this flattening becomes too great, the drop becomes unstable to small disturbances and breaks apart. The Weber number relates the dynamic pressure and surface tension.

$$We = \frac{\rho V^2 r}{\tau_s} = \frac{\rho_o V_\infty{}^2 r_\infty}{\tau_s} \left(\bar{\rho}\bar{V}^2\bar{r}\right) \tag{20}$$

Chapman and Larson (ref. 9) note that for Weber numbers up to about 1.1, the departure from spherical shape should be trivial. The appropriate value of the Weber number for breakup is uncertain. Chapman and Larson used

$$We = 2.6 \tag{21}$$

as the value for incipient disruption of a tektite drop, but it certainly is possible that a larger value would be more appropriate. The viscosity of the molten meteoric material plays an important role in this regard. For example, for molten iron the appropriate value would be perhaps 2 or less since the kinematic viscosity is very low. In the results presented later there are plots showing the values of the entry parameters that lead to values of $We \cos Z_R$ equal to 1.1, 2.5, and 4.0.

Finally, the luminous intensity is defined by the usual relation (e.g., ref. 2)

$$I = -\frac{1}{2}\tau_o V^3 \frac{dm}{dt} \tag{22}$$

Let us define a luminous intensity coefficient as

$$i = \frac{2I}{\tau_o V_\infty{}^3 m_\infty} = -\bar{V}^3 \frac{d\bar{m}}{dt} \tag{23}$$

With assumptions (1) and (2) this becomes

$$i = 3V_\infty \cos Z_R \left(\bar{V}^4 \bar{r}^2 \frac{d\bar{r}}{dh}\right) \tag{24}$$

RESULTS

The foregoing equations were solved on an electronic computer. Results were obtained for the four meteoroid materials with the product $r_\infty \cos Z_R$ varying from 0.01 μ to 5 mm.

The results are generally presented as if $r_\infty \cos Z_R$ were, in fact, a proper similarity variable, which it is not when the temperature difference between the front and rear face becomes important, since this difference is determined by r_∞ rather than $r_\infty \cos Z_R$. A few check calculations indicated that the errors introduced by this treatment were small, as will be shown later, so that for practical purposes the variable may be considered a proper one even though the results rigorously apply only when $\cos Z_R$ is equal to unity.

For all of the materials except tektite the assumed entry velocities range from 11 to 70 km/sec. For the tektites the range chosen was 11 to 30 km/sec. The higher speed results for stone and iron are only included to make the trends with speed self-evident.

The results presented in figures 1 through 8 are for tektite, figures 9 through 23 for stone, figures 24 through 32 for pumice, and figures 33 through 41 for iron. For each of these materials at the various speeds and for the full range of $r_\infty \cos Z_R$ the following results are given: (1) front surface maximum temperature, (2) rear surface maximum temperature, (3) altitude range for which the molten state exists, (4) ratio of final size to size at entry, (5) altitude at which the speed has dropped to 500 m/sec, (6) values of $i_{max}/\cos Z_R$, (7) altitude for maximum luminous intensity, and (8) the solid-liquid boundary as well as information on $\psi \cos Z_R$ and $We \cos Z_R$ to indicate the likely limits of applicability of the results. Some additional figures are included which give other quantities that are useful to the discussion.

In the case of luminous intensity, it is of value to compare the results of the computations with the predictions of a simplified theory which assumes that no radiation from the body occurs. The "ablation-only" theory in question is treated in the appendix.

DISCUSSION AND CONCLUDING REMARKS

In the following discussion of results we will, in a number of instances, compare the present machine calculated results with the predictions of usual meteor theory, which assumes that ablation alone is the cooling mechanism and that the atmospheric density varies exponentially with altitude:

$$\bar{\rho} = \frac{\rho}{\rho_o} = e^{-\beta h} \tag{25}$$

The inverse scale height, β, is not constant, in fact, but varies as shown in figure 42, which was plotted using data from the 1962 U. S. Standard Atmosphere (ref. 6). Because β does vary with altitude, it is to be expected that better agreement between the machine calculated results and theory would be obtained if in the latter at any given altitude of interest a local value of β (herein denoted as β') appropriate to that altitude were used in the comparison. The value β' can be found as follows: Differentiating equation (25) with β as a function of h gives

$$\frac{d\bar{\rho}}{dh} = -e^{-\beta h}\left(\beta + h\frac{d\beta}{dh}\right) = -\bar{\rho}\left(\beta + h\frac{d\beta}{dh}\right) \tag{26}$$

so that

$$\beta' = \beta + h\frac{d\beta}{dh} = -\frac{d\bar{\rho}/dh}{\bar{\rho}} \tag{27}$$

Values of β' have been determined for the U. S. Standard Atmosphere 1962 using the tabulated values (ref. 6) of $\bar{\rho}$ and $d\bar{\rho}/dh$ averaged over a 1 km height. These values are also plotted in figure 42. Note that the β' variation with altitude is somewhat erratic even though the method used for obtaining $d\bar{\rho}/dh$ tends to smooth out the variation. That is, the densities given in this standard atmosphere do not fall on a smooth curve, and as we shall see, this fact reflects itself in certain of the results presented.

When comparisons are made with theory assuming an average value of β, this value has been chosen as 1.45×10^{-4} m^{-1}.

At the outset it is necessary to establish how well the product $r_\infty \cos Z_R$ fits as a fundamental similarity variable. As noted earlier when front and rear temperatures differ, the product $r_\infty \cos Z_R$ is not a proper variable. The adequacy of treating it as such can be determined by examining the effect of changing $\cos Z_R$ from unity to some small value for a material for which large differences between front and rear surface temperatures occur. Of the four materials studied, pumice is such a material. To find the results for pumice values of $\cos Z_R$ of 0.3 as well as unity were used. The deviation of results was significant only for those quantities shown in figures 25, 27, and 32. The dashed curves show the effect of reducing $\cos Z_R$ to 0.3 at 11, 30, and 70 km/sec. The differences are significant only for the ratio of maximum-to-minimum drag coefficient at the higher speeds and for the rear surface temperatures at the lower speeds.

The numerical results indicated that the effect of ablation on drag coefficient was important only for pumice and then only for the larger sizes. For that reason the ratio of maximum-to-minimum drag coefficient as a function of entry size and speed for the pumice only is shown (fig. 32).

Consider, now, the variation of the maximum front and rear surface temperatures with entry size and speed (see figs. 1, 2, 9, 10, 24, 25, 33, and 34). These variations are about what one would expect. The plot of figure 43

serves to assist in comparing the differences that do exist for the four materials at a common entry speed (30 km/sec). For sizes of 1 micron and less, radiative cooling predominates so that

$$\frac{dq}{dt} = \frac{1}{2} \lambda \rho V^3 A = 4\epsilon\sigma T^4 A \tag{28}$$

Then it may be shown (e.g., using the analysis of ref. 10 which assumes no ablation) that for a given entry speed

$$T^4_{max} \sim \beta \rho_m r_\infty \cos Z_R \tag{29}$$

This agrees with the results presented in figure 43 if the local inverse scale height, β', is used in place of β.

As the sizes are increased into the range wherein ablation affects the results, it will be noted that the tektite temperatures become relatively high when compared with those of the other materials. This occurs because the ablation rate at a given temperature is less than that for the other materials (see values of c_1 and c_2 of table I).

A comparison for each of the materials of the size at which the maximum front and rear temperatures depart from each other is somewhat surprising in that, although the thermal conductivities of the materials are greatly different, the "departure" size differences are not great. The conductivity of the iron is 400 times greater for the pumice but the departure size is only one order of magnitude larger.

Before leaving the subject of maximum front surface temperature it should be pointed out that, except for stone and tektite, the results may be subject to future readjustment. For pumice the ablation parameters c_1 and c_2 may differ considerably from the values used (the same as for stone). For iron no allowance was made for heat addition resulting from oxidation, that theory indicates (ref. 11) and experiment shows (ref. 12) will occur. Thus for the larger sized irons the actual temperatures should exceed somewhat the values shown.

One final comment concerning maximum rear surface temperatures is in order. For pumice only there exists a rather large range of entry sizes and speeds for which no rear surface melting occurs, although for tektite at the lowest speeds (which Chapman's analyses indicate to be the most likely) the rear surface would be a very viscous fluid for a narrow range of size.

Examination of the plots of the ratio of final radius to initial radius as a function of entry size and speed (figs. 4, 12, 27, and 36) shows that the transition from the case for which radiative cooling dominates ($r_o/r_\infty = 1$) to that for which ablative cooling dominates takes place within a rather small change in entry size. This is particularly evident at the highest entry speeds wherein the transition is essentially complete with one order of magnitude change in entry radius. The plots of $\overline{V}$ versus $\overline{r}$ for stone at 30 km/sec

(fig. 17) are characteristic of the manner in which the size of all the materials changes. The dashed curve gives the theoretical variation when ablative cooling only occurs. (See appendix, eq. (A3).)

The variation of the maximum luminous intensity coefficient with size and speed has some interesting features. (See figs. 6, 14, 29, and 38.) As entry size decreases from the maximum of the study, the coefficient generally increases somewhat erratically to a maximum and then rather abruptly falls to a trivial value. This erratic behavior is evidently due to the fact that the standard atmospheric density variations with altitude given by reference 6 are themselves erratic, as was mentioned earlier. The peaking characteristic, which was not expected, cannot be explained by variations in the local values of β as is shown (fig. 18) for the example case of stones entering the atmosphere at 30 km/sec. (On this and some subsequent figures the calculated points are included to show how the curves were faired.) The peaking behavior can be explained as follows: From equation (23)

$$i = -\bar{V}^3 \frac{d\bar{m}}{dt} \tag{30}$$

and for ablative cooling only (see appendix, eq. (A1))

$$\frac{d\bar{m}}{dt} \sim -\bar{\rho}\bar{V}^3\bar{r}^2 \tag{31}$$

so that

$$i \sim \bar{\rho}\bar{V}^6\bar{r}^2 \tag{32}$$

Bodies with entry radii of order 10^{-5} m, which at the higher altitudes are primarily cooled by radiation, remain larger throughout the trajectory than they would if ablation were the sole cooling means, as noted earlier. In particular, the size at the altitude for maximum luminous intensity is larger (see fig. 19) but, more importantly, the altitude itself (see fig. 20) is so much lower than predicted for the case of ablation cooling only that the corresponding air density is considerably greater. Thus, although the velocity at peak luminous intensity is somewhat lower (see fig. 21), the product $\bar{\rho}\bar{V}^6\bar{r}^2$ is much larger than theory for ablative cooling only predicts. When the theoretical values of luminous intensity using the local β are corrected for the change in this product, the results (fig. 18) provide some explanation for the peaking trend observed. Altogether, the peaking can be attributed to the existence of radiative cooling, which causes a deeper penetration into the atmosphere than would otherwise occur.

The variations of maximum luminous intensity discussed above are only of academic interest since meteor magnitude is determined by the logarithm of intensity and the variation of the logarithms of the maximum luminous intensity coefficient is small as may be seen, for example, in figure 22. This figure shows how photographic or visual meteor absolute magnitude varies with altitude for the various sizes of stone bodies for the common entry speed of 30 km/sec. A more instructive plot is that of figure 23 wherein the

magnitudes and altitudes are normalized with respect to the maximum magnitude and altitude at maximum magnitude. On this plot one can compare the results with theory for ablative cooling only. The differences shown are about what one would expect.

The appearance of figure 23 is of interest in another connection. Deviations of the light curve from the results of pure ablation theory of the type shown are commonly observed in the case of faint meteors (see refs. 13-15). Cook (ref. 13) attributed such deviations to surface radiation. Later Jacchia (ref. 14) showed that fragmentation would cause a similar behavior. The fragmentation explanation seems to have been widely accepted (see, e.g., refs. 5 and 15). It is probable that the explanation based on surface radiation is the correct one for many of the faint meteors that have been observed.

Some comments are in order on the limits of applicability of the analysis with respect to both departure from free molecular flow and freedom from drop breakup resulting from excessive dynamic pressure.

Departure from free molecular flow occurs only as a result of interaction between vapor molecules from the front face with the air molecules since in no case did the Knudsen number fall below unity until that portion of the trajectory was reached wherein the speeds had dropped to very low values. The screening factor values, $\psi_{max} \cos Z_R$, are given in figures 8, 16, 31, and 40 for the four materials, and they show that the analysis should be valid for $r_\infty \cos Z_R$ to about 100 μ.

Drop breakup does not impose a limit until the size is increased to nearly 1 mm as shown by the plotted Weber numbers. In fact, for slow speed tektites, and particularly for the pumices, drop breakup may not be a factor if, as indicated, the rear face of the body is solid or essentially so.

A final comment is in order concerning a question raised in the introduction regarding the compatibility of the calculated final size of irons presented with the known iron meteorite size-abundance relation found from cosmic dust collection.

Figure 41 presents the meteorite size ($r_o \cos Z_R$) as a function of entry size for entry speeds of 20 and 30 km/sec which should bracket the probable entry speed range for such meteoroids. As was noted previously the values of $r_o \cos Z_R$ for the larger entry sizes might well be too big because in the analysis no account was taken of additional ablation resulting from heat addition due to oxidation. With this restriction in mind and the fact that the average value for the cosine Z_R can be shown to be two-thirds, the expectation from these results is that the maximum radius of iron cosmic dust should be greater than a few microns and not much more than the order of 20 μ. This result is in good agreement with the results of collection counts (see ref. 16).

Ames Research Center
National Aeronautics and Space Administration
Moffett Field, Calif., March 18, 1965

APPENDIX A

ANALYSIS OF ENTRY INTO AN ISOTHERMAL ATMOSPHERE WITH ABLATIVE COOLING ONLY

If the meteoric body is cooled only by ablation, then

$$\zeta \frac{dm}{dt} = -\frac{1}{2} \lambda \rho V^3 a \tag{A1}$$

Assuming an isothermal atmosphere together with assumptions (1) and (2) leads to

$$\frac{d\overline{r}}{dh} = \frac{\rho_o \lambda V_\infty^{\ 2}}{8\rho_m \zeta r_\infty \cos Z_R} \left(\overline{V}^2 e^{-\beta h}\right) \tag{A2}$$

With equation (3) then one obtains Öpik's equation

$$\overline{r} = e^{-\eta(1-\overline{V}^2)} \tag{A3}$$

where

$$\eta = \frac{\lambda V_\infty^{\ 2}}{12\gamma\zeta} \tag{A4}$$

From equations (3) and (A3) one can show that

$$\overline{\rho} = e^{-\beta h} = \frac{2\beta\rho_m r_\infty \cos Z_R}{3\gamma\rho_o} \left\{e^{-\eta}\left[\overline{Ei}(\eta) - \overline{Ei}(\eta\overline{V}^2)\right]\right\} \tag{A5}$$

where $\overline{Ei}$ denotes the exponential integral (for tabulated values see ref. 17).

Substituting equations (A2), (A3), and (A5) in equation (24) gives

$$\frac{i}{\beta V_\infty \cos Z_R} = \frac{3e^{-3\eta}\, e^{2\eta\overline{V}^2} (\eta\overline{V}^2)^3}{\eta^2} \left[\overline{Ei}(\eta) - \overline{Ei}(\eta\overline{V}^2)\right] \tag{A6}$$

The maximum value of $i/\beta V_\infty \cos Z_R$ and the corresponding values of $\overline{V}$, $\overline{r}$, and

$$\xi = \frac{\gamma\rho}{\beta\rho_m r_\infty \cos Z_R} = \frac{2}{3} e^{-\eta}\left[\overline{Ei}(\eta) - \overline{Ei}(\eta\overline{V}^2)\right] \tag{A7}$$

have been calculated and are given in table II.

REFERENCES

1. Cook, A. F.; Jacchia, L. G.; and McCrosky, R. E.: Luminous Efficiency of Iron and Stone Asteroidal Meteors. Smithsonian Contributions to Astrophysics, Proc. Symposium on the Astronomy and Physics of Meteors, vol. 7, 1963, pp. 209-20.

2. Allen, H. Julian; and James, Nataline A.: Prospects for Obtaining Aerodynamic Heating Results From Analysis of Meteor Flight Data. NASA TN D-2069, 1964.

3. Whipple, Fred L.: The Theory of Micro-Meteorites. Part 1. In an Isothermal Atmosphere. Proc. Natl. Acad. Sci., vol. 36, no. 12, Dec. 15, 1950, pp. 687-95.

4. Chapman, Dean R.: On the Unity and Origin of the Australasian Tektites. Geochimica et Cosmochimica Acta, vol. 28, no. 6, June 1964, pp. 841-80.

5. Öpik, Ernst J.: Physics of Meteor Flight in the Atmosphere. Interscience Tracts on Physics and Astronomy No. 6. Interscience Pub., N.Y., 1958.

6. Anon.: GPO U. S. Standard Atmosphere, 1959 and 1962. Wash., D. C., Dec. 1962.

7. Levin, B. I.: Physikalische Theorie der Meteore und die Meteoritische Substanz in Sonnensystem. Translated from Russian to German by N. Richter. Akademie-Verlag, Berlin, 1961.

8. Scala, S. M.; and Vidale, G. L.: Vaporization Processes in the Hypersonic Laminar Boundary Layer. Int. J. Heat and Mass Trans., vol. 1, no. 1, June 1960, pp. 4-22.

9. Chapman, Dean R.; and Larson, Howard K.: The Lunar Origin of Tektites. Paper presented at the XIII International Astronautical Congress, Varna, Bulgaria, Sept. 23-29, 1962.

10. Allen, H. Julian; and Eggers, Alfred J., Jr.: A Study of the Motion and Aerodynamic Heating of Ballistic Missiles Entering the Earth's Atmosphere at High Supersonic Speeds. NACA Rep. 1381, 1958. (Supersedes NACA TN 4047.)

11. Cook, M. A.; Eyring, H.; and Thomas, R. N.: The Physical Theory of Meteors. I. A Reaction-Rate Approach to the Rate of Mass Loss in Meteors. Astrophys. J., vol. 113, no. 3, May 1951, pp. 475-81.

12. Schmidt, Richard A.; Keil, Klaus; and Gault, Donald E.: Electron Microprobe Study of a Crater and Ejecta Produced by Hypervelocity Impact Against a Ni-Fe Target. Proc. Seventh Hypervelocity Impact Symposium, Tampa, Florida, Nov. 17-19, 1964.

13. Cook, A. F.: The Physical Theory of Meteors VI. The Light Curve. Astrophys. J., vol. 120, 1954, pp. 572-7.

14. Jacchia, Luigi G.: The Physical Theory of Meteors. VIII. Fragmentation as Cause of the Faint-Meteor Anomaly. Astrophys. J., vol. 121, 1955, pp. 521-7.

15. Hawkins, Gerald S.; and Southworth, Richard B.: The Statistics of Meteors in the Earth's Atmosphere. Smithsonian Contributions to Astrophysics, vol. 2, no. 11, 1958, pp. 349-64.

16. Hodge, Paul W.; Wright, Frances W.; and Langway, Chester C., Jr.: Studies of Particles for Extraterrestrial Origin - Part 3 - Analyses of Dust Particles From Polar Ice Deposits. J. Geophys. Res., vol. 69, no. 14, July 15, 1964, pp. 2919-31.

17. National Bureau of Standards: Tables of Sine, Cosine, and Exponential Integrals, Vols. I and II. Prepared by the Federal Works Agency, Work Projects Adm. for the City of New York, 1940.

TABLE I.- PERTINENT CONSTANTS FOR METEORIC MATERIAL

Quantity	Iron	Stone	Tektite	Pumice
M	56	50	42	50
$^{\dagger}c_1$	9.607	9.600	13.301	9.600
$^{\dagger}c_2$	-1.612×10^4	-1.350×10^4	-2.5102×10^4	-1.350×10^4
ζ, $m^2\ sec^{-2}$	8.01×10^6	7.98×10^6	14.98×10^6	7.98×10^6
ρ_m, $kg\ m^{-3}$	7.8×10^3	3.4×10^3	2.4×10^3	4×10^2
τ_s, $kg\ sec^{-2}$	1.20	0.36	0.36	0.36
k, $W\ m^{-1}\ {}^{\circ}K^{-1}$	40.0	2.0	1.6	0.1
T_f, ${}^{\circ}K$	1.8×10^3	1.8×10^3	1.8×10^3	1.8×10^3

†These values apply if p_v is given in $N\ m^{-2}$ and for T in ${}^{\circ}K$.

TABLE II.- VALUES OF $\xi_{i_{max}}$ AND RELATED QUANTITIES

[Note 0.4 - 2 = 0.4×10^{-2}]

η	$\bar{r}_{i_{max}}$	$\bar{V}_{i_{max}}$	$i_{max}/\beta V_\infty \cos Z_R$	$\xi_{i_{max}}$
0	1.0000	0.84645	0	0.2222-0
.2	.9500	.86249	.06422	.1920-0
.5	.8950	.88217	.13411	.1579-0
1.0	.8361	.90608	.20897	.1200-0
1.5	.7999	.92260	.25568	.9598-1
2.0	.7760	.93444	.28728	.7962-1
2.5	.7590	.94323	.30997	.6792-1
3.0	.7465	.95002	.32701	.5912-1
4.0	.7294	.95975	.35084	.4687-1
5.0	.7182	.96634	.36668	.3879-1
6.0	.7104	.97109	.37795	.3307-1
7.0	.7046	.97467	.38638	.2881-1
8.0	.7003	.97748	.39291	.2551-1
9.0	.6967	.97972	.39813	.2290-1
10.0	.6939	.98156	.40239	.2076-1
12.0	.6896	.98439	.40892	.1750-1
14.0	.6865	.98648	.41370	.1512-1
16.0	.6841	.98806	.41735	.1331-1
18.0	.6822	.98932	.42022	.1189-1
20.0	.6806	.99033	.42254	.1074-1
22.0	.6793	.99118	.42446	.9796-2
24.0	.6781	.99188	.42607	.9003-2
26.0	.6773	.99248	.42744	.8327-2
30.0	.6759	.99346	.42964	.7240-2
35.0	.6746	.99436	.43171	.6228-2
40.0	.6737	.99505	.43327	.5461-2
45.0	.6730	.99559	.43448	.4865-2
50.0	.6725	.99602	.43546	.4384-2
60.0	.6717	.99668	.43694	.3611-2
∞	.6667	1.00000	.44144	0

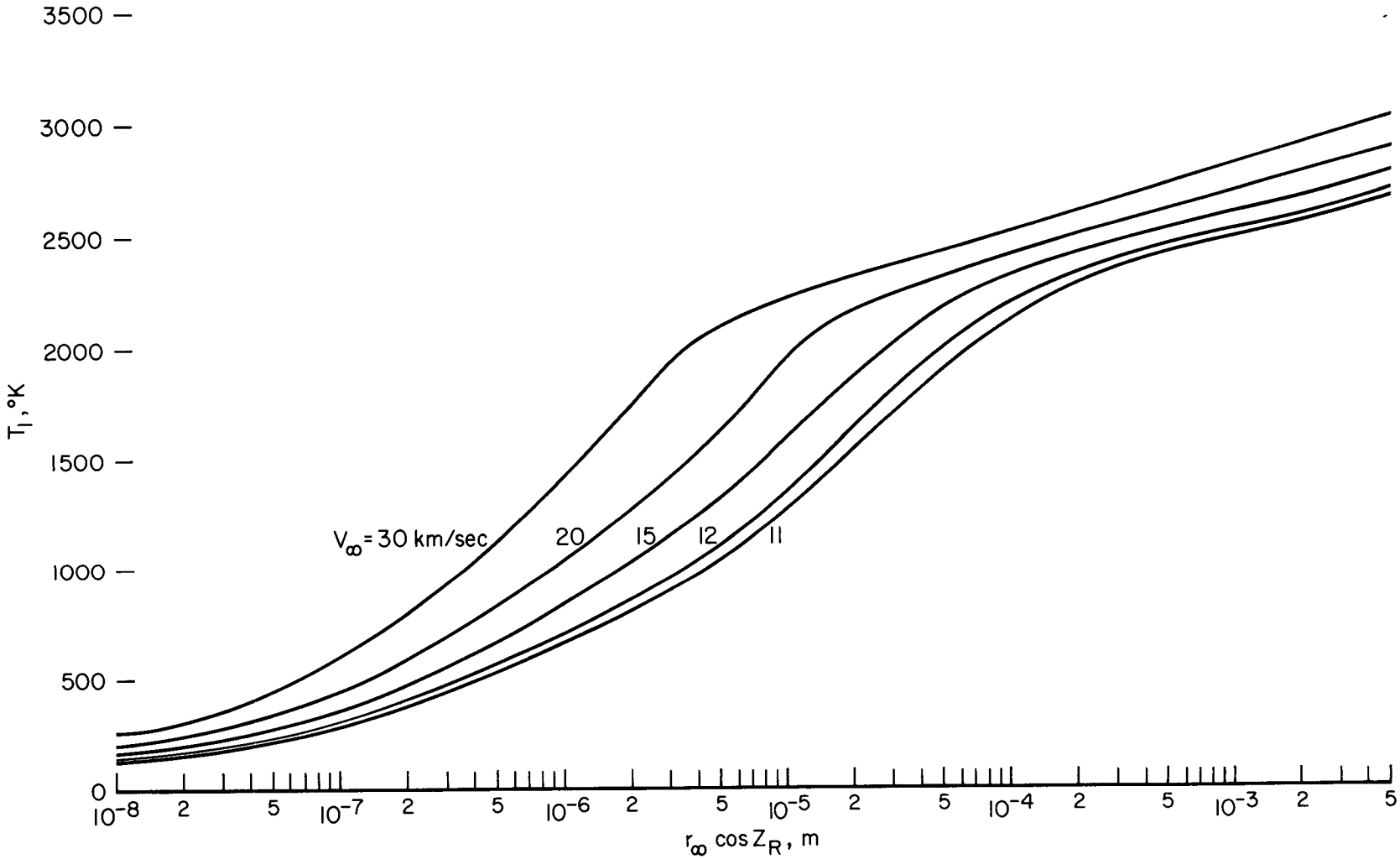

Figure 1.- Front face maximum temperature, T_1, for tektite.

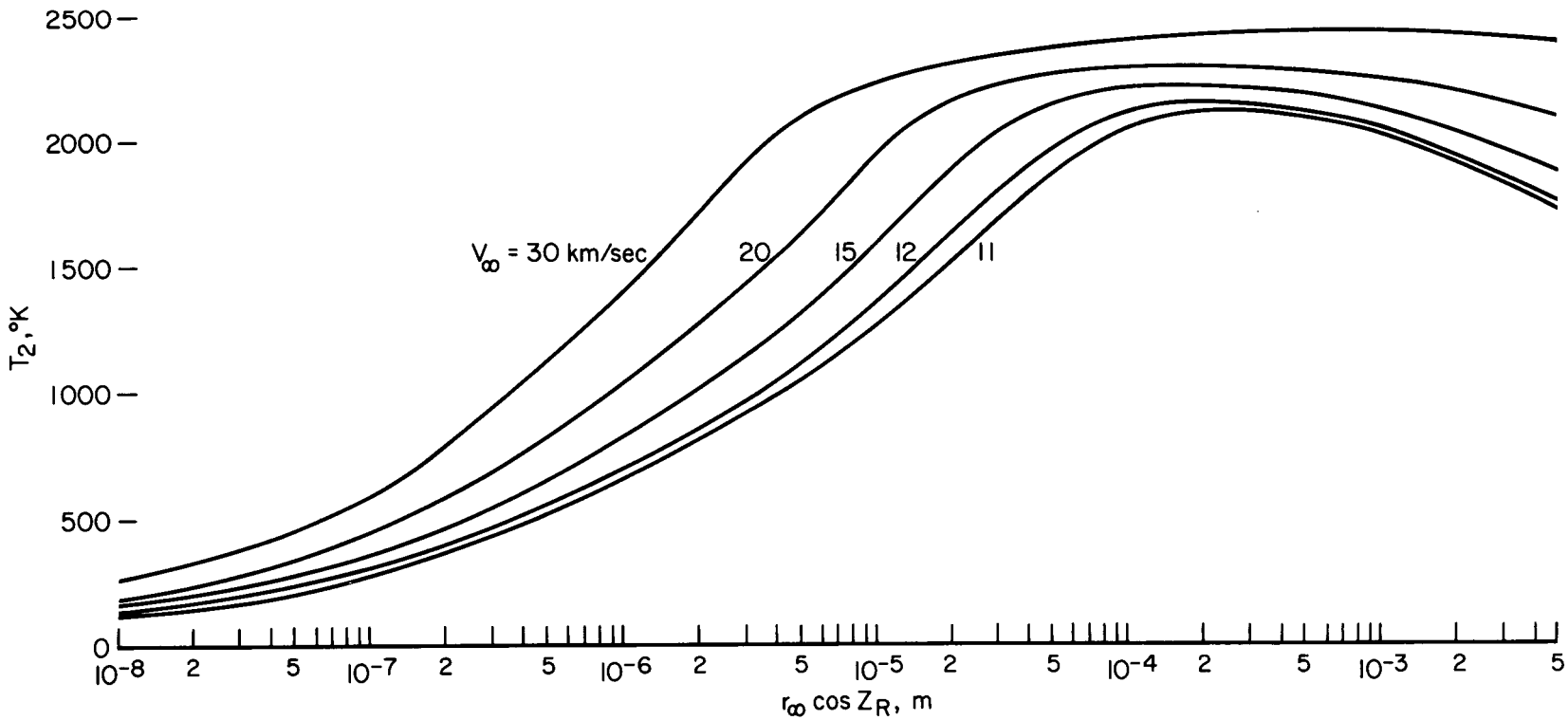

Figure 2.- Rear face peak temperature, T_2, for tektite.

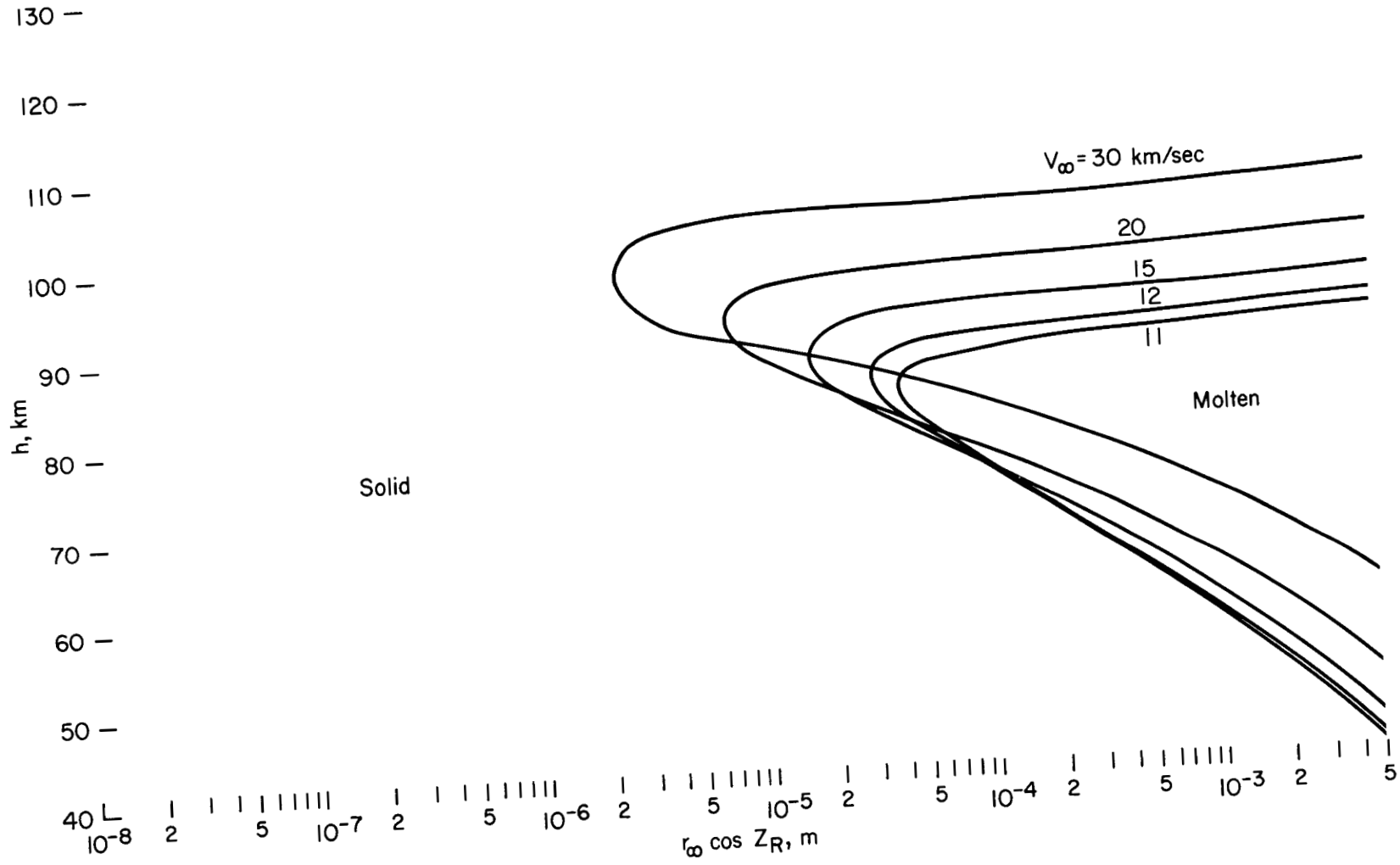

Figure 3.- Front face melting zone for tektite.

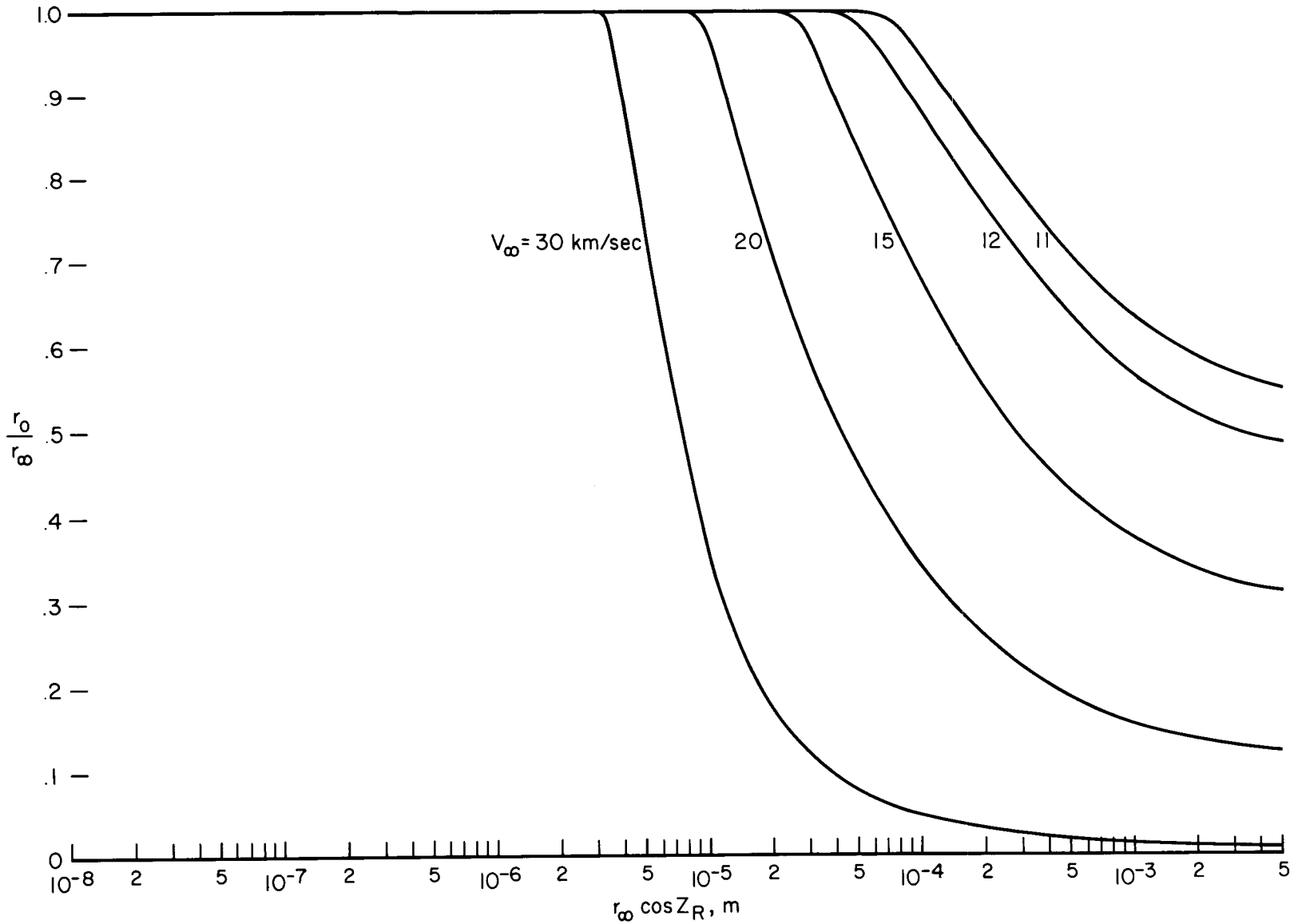

Figure 4.- Ratio of final to entry radius, r_o/r_∞, for tektite.

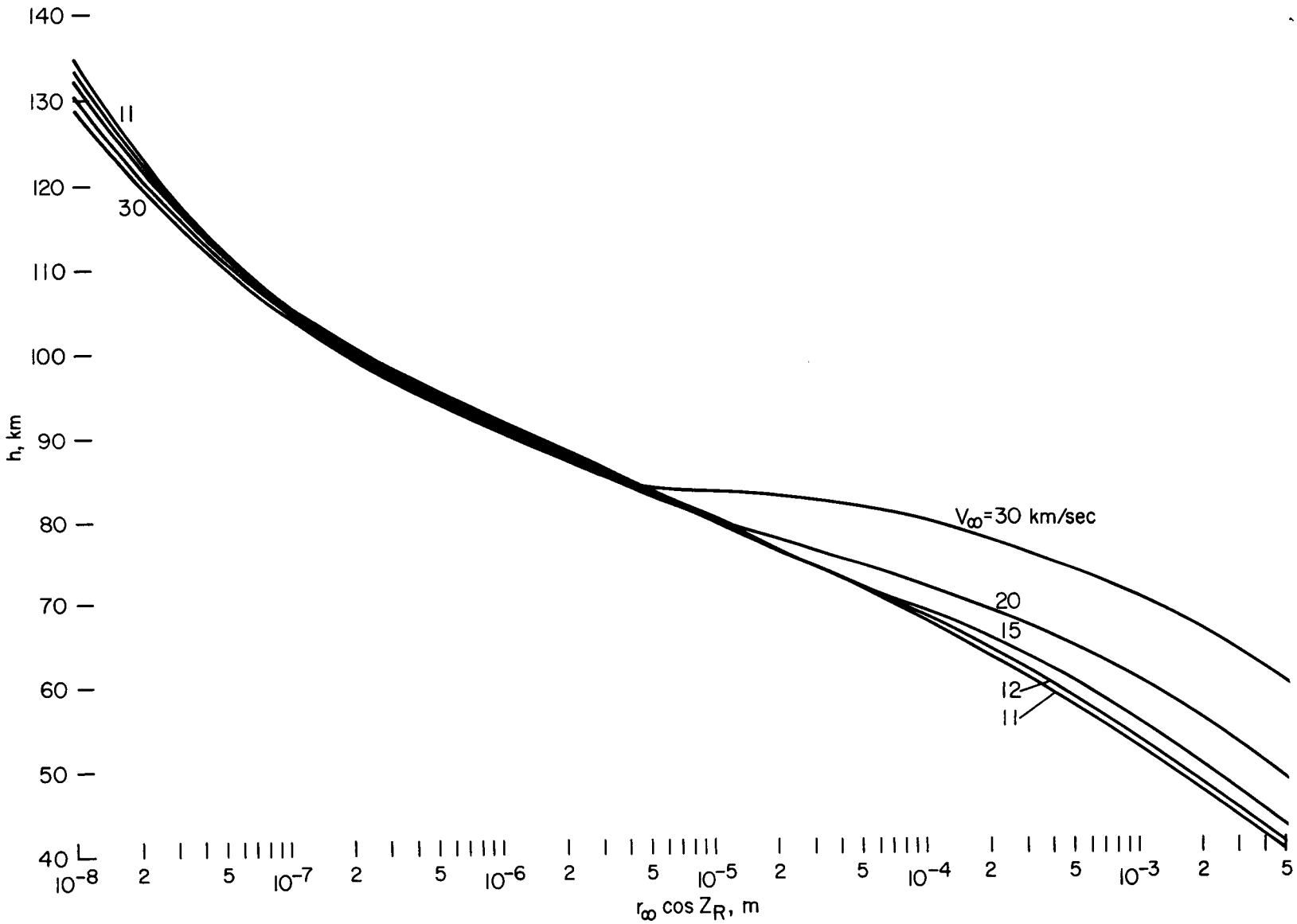

Figure 5.- Final altitude (V = 500 m/sec) for tektite.

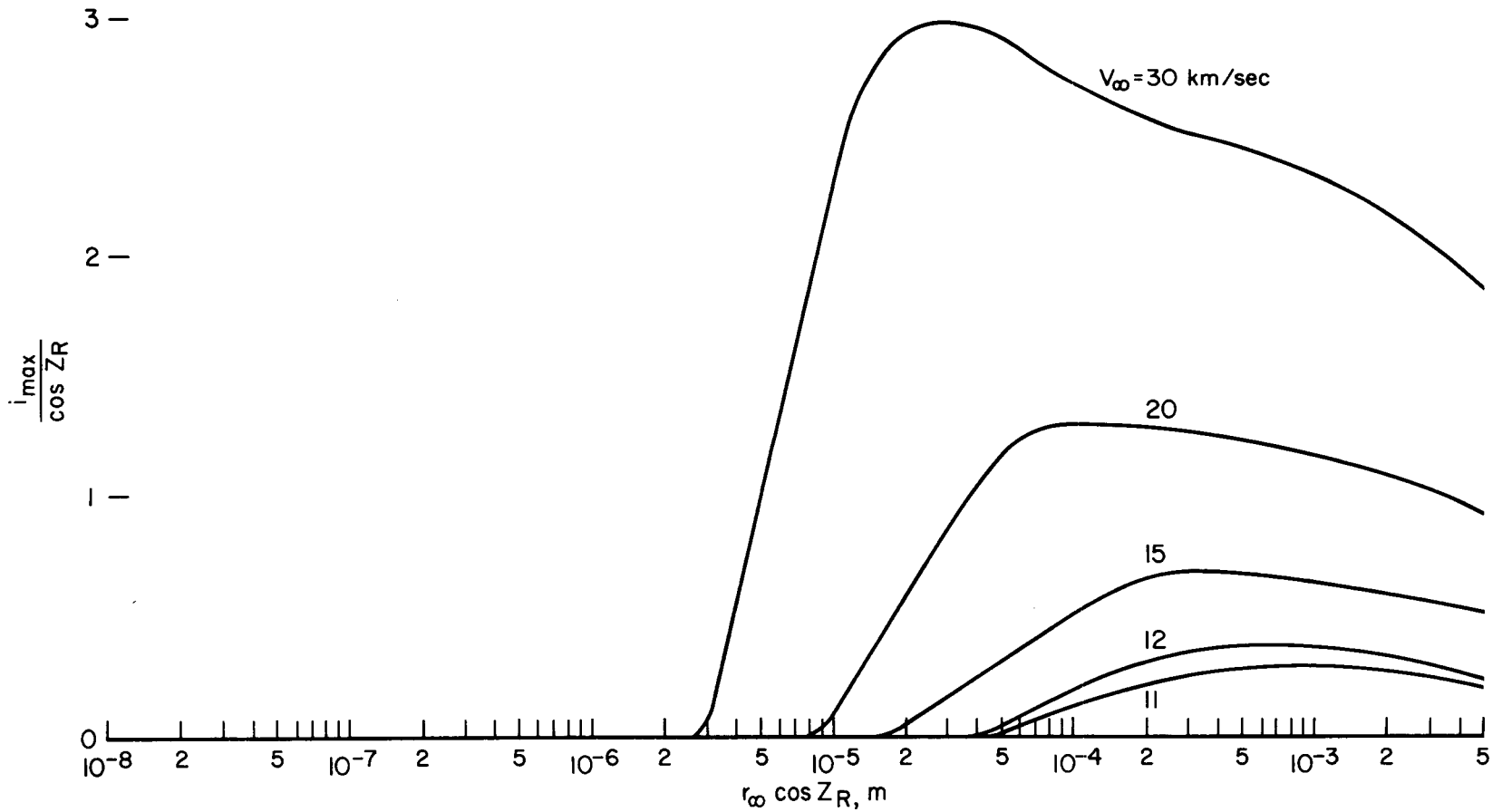

Figure 6.- Maximum luminous intensity coefficient for tektite.

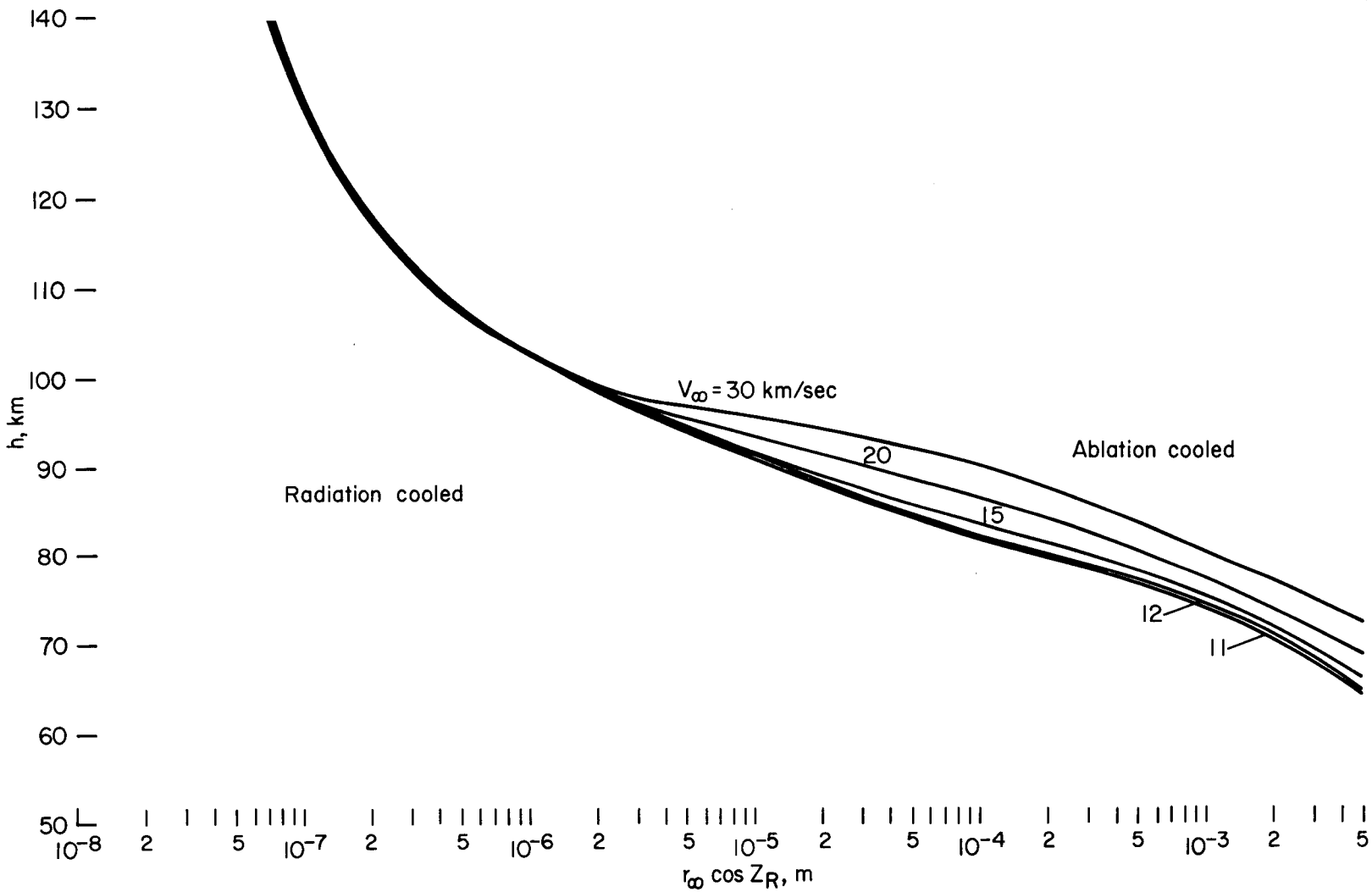

Figure 7.- Altitude at maximum luminous intensity for tektite.

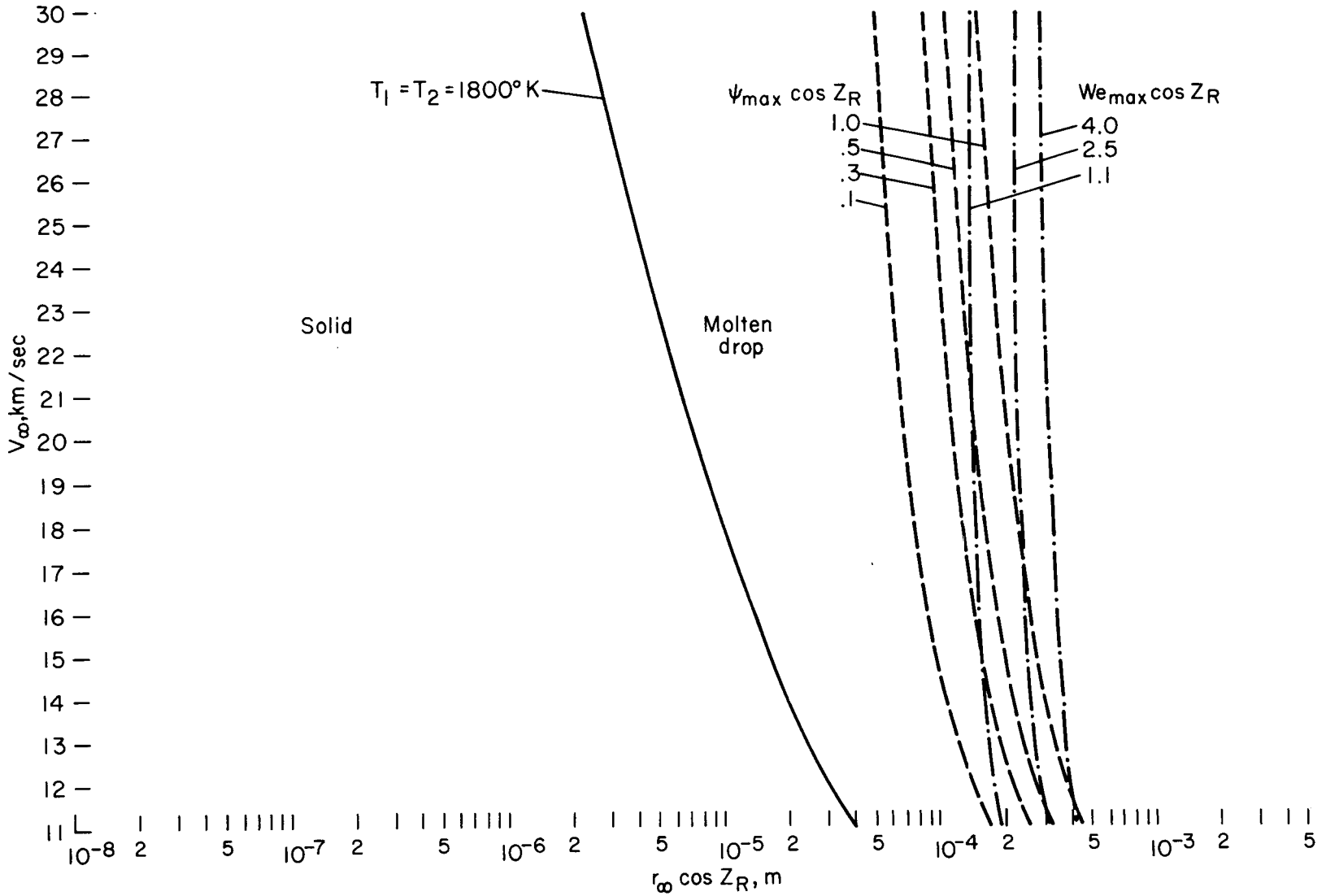

Figure 8.- Limits of validity of analysis for tektite.

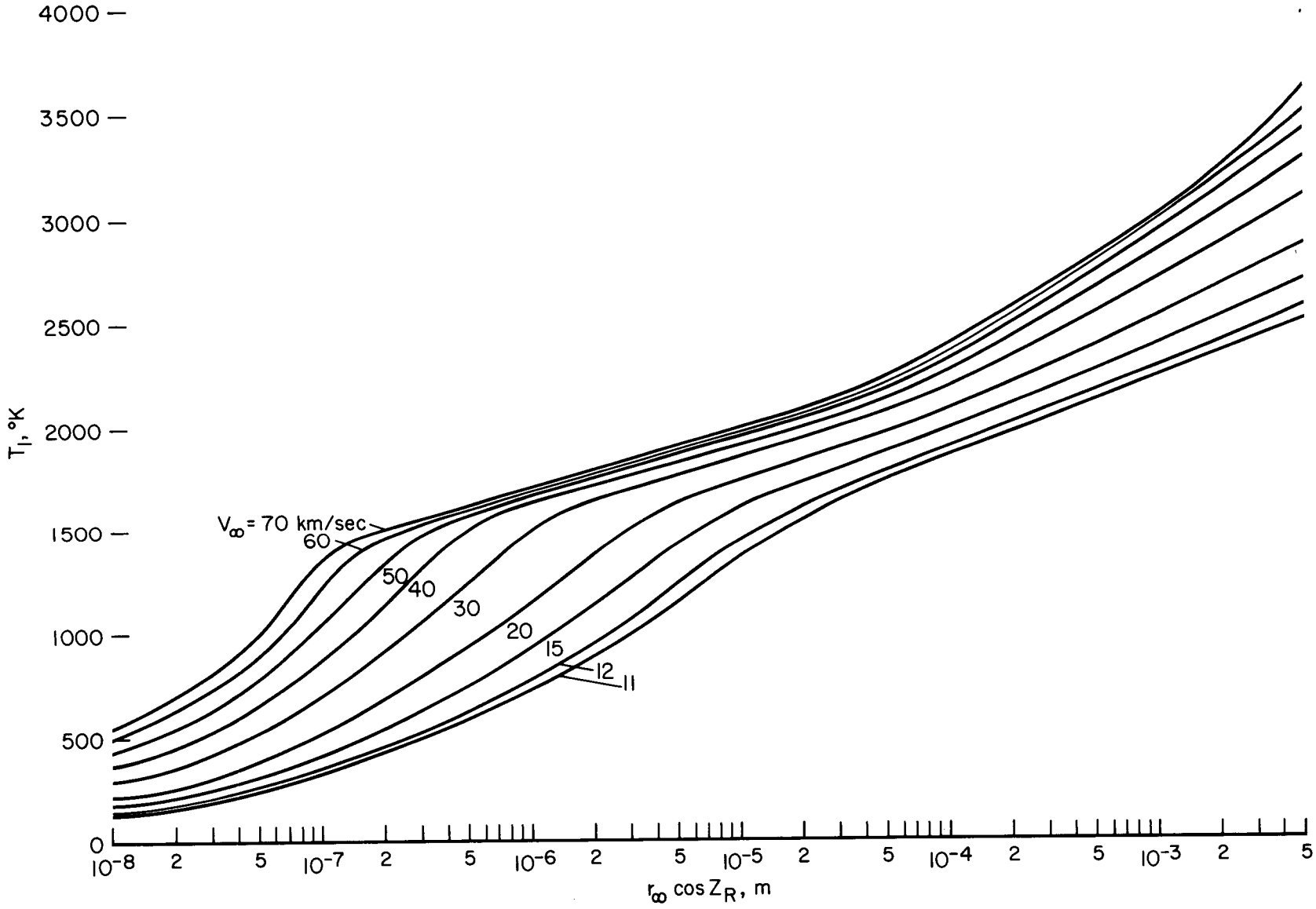

Figure 9.- Front face maximum temperature, T_1, for stone.

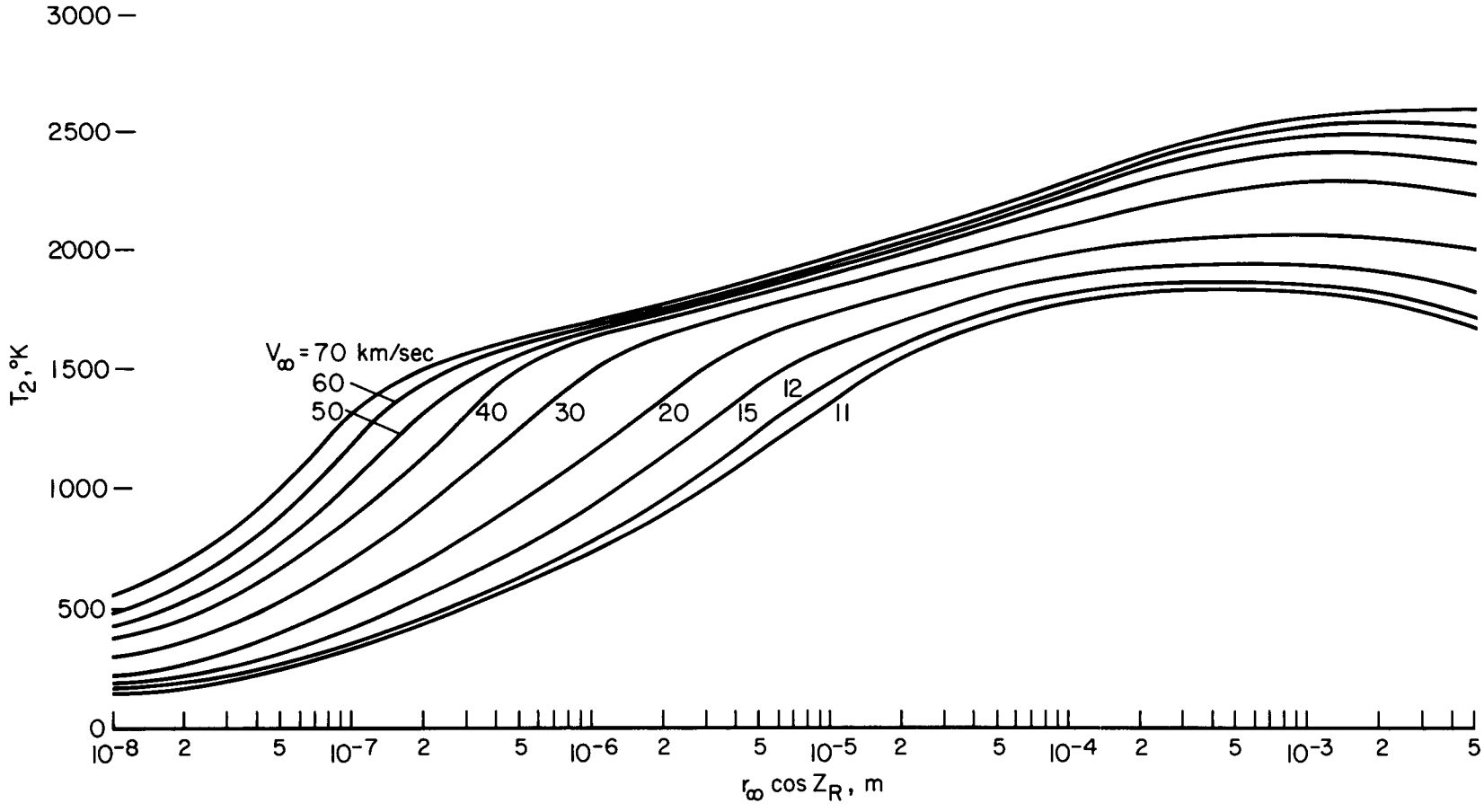

Figure 10.- Rear face maximum temperature, T_2, for stone.

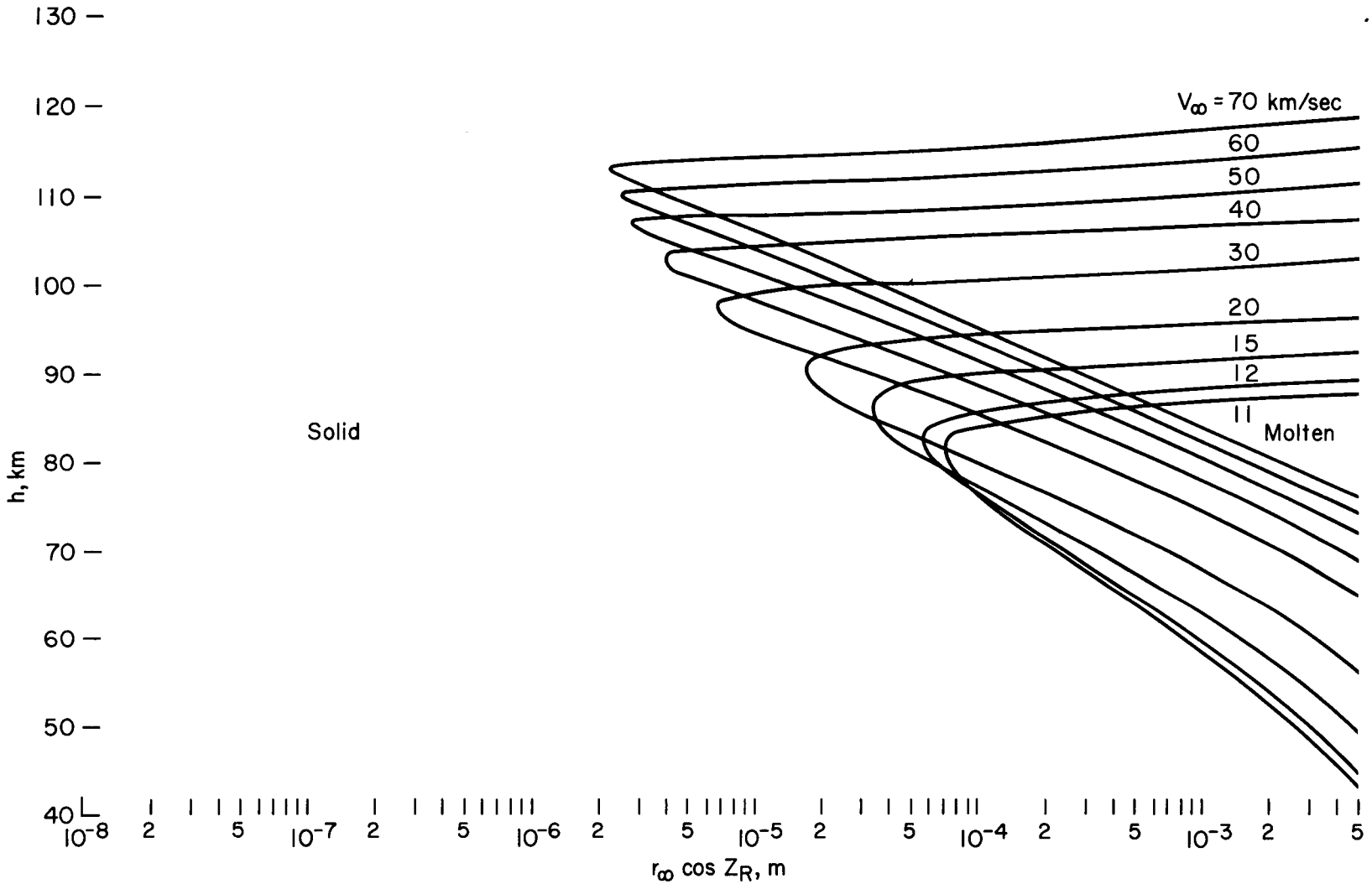

Figure 11.- Front face melting zones for stone.

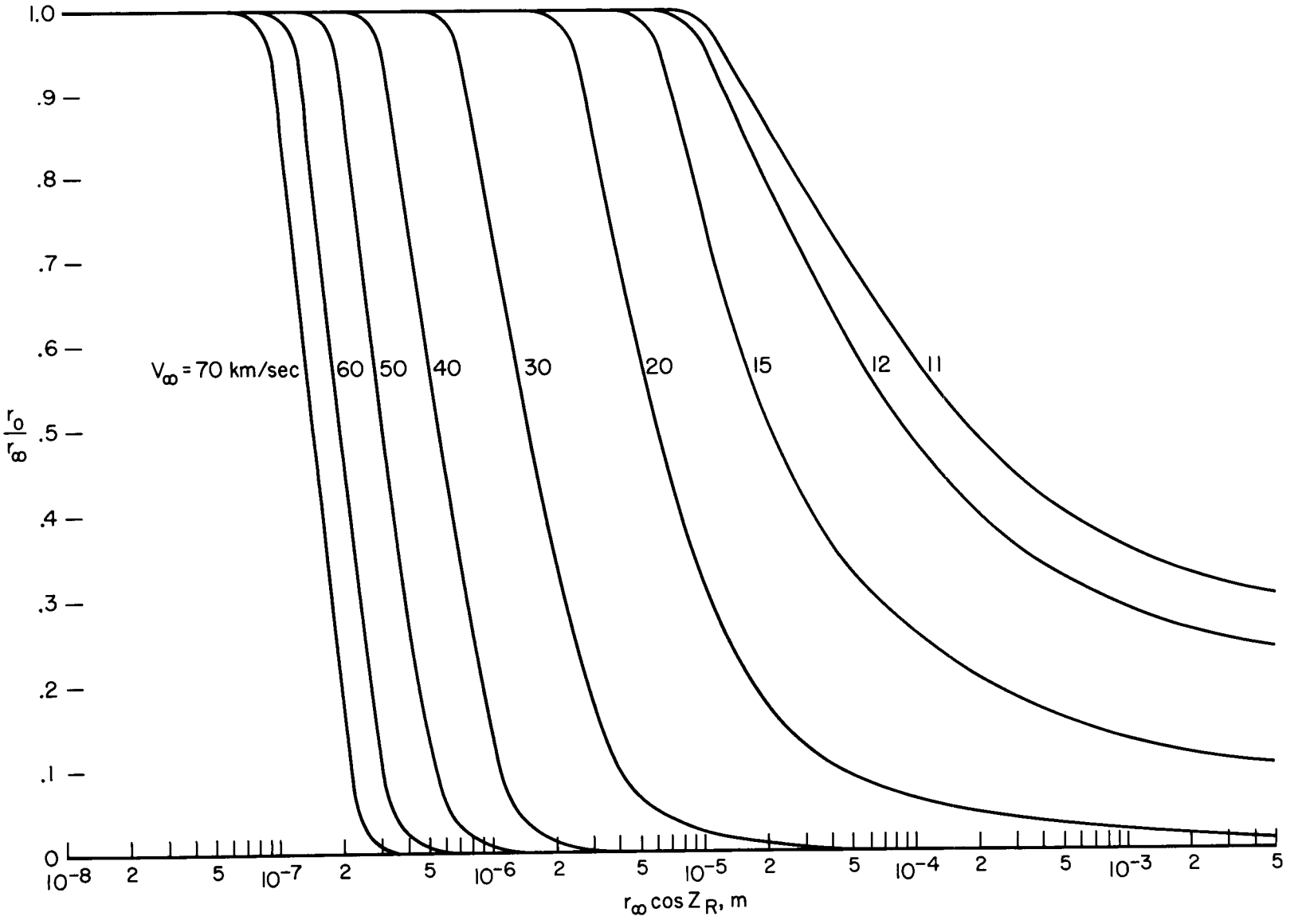

Figure 12.- Ratio of final to entry radius, r_o/r_∞, for stone.

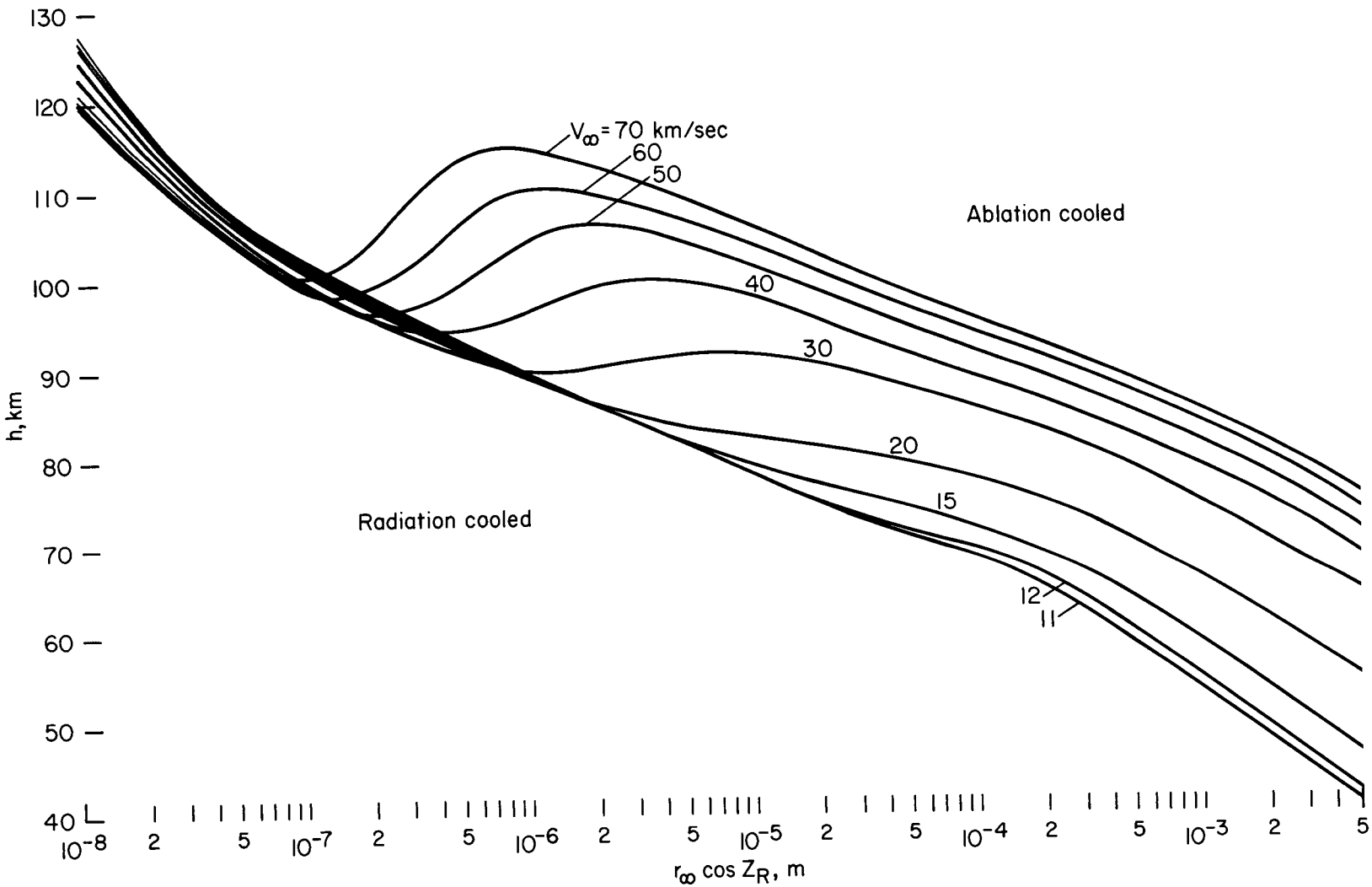

Figure 13.- Final altitude (V = 500 m/sec) for stone.

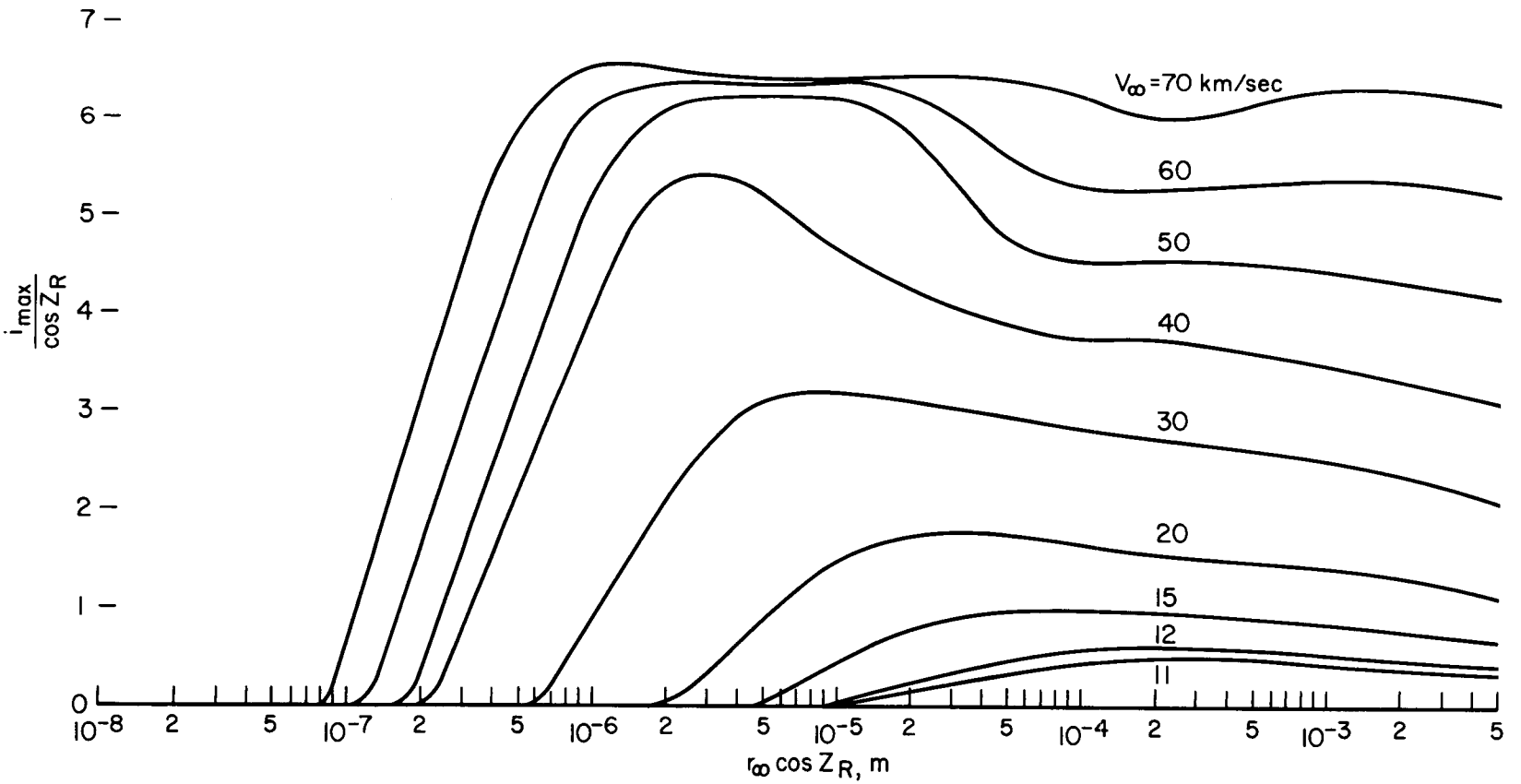

Figure 14.- Maximum luminous intensity coefficient for stone.

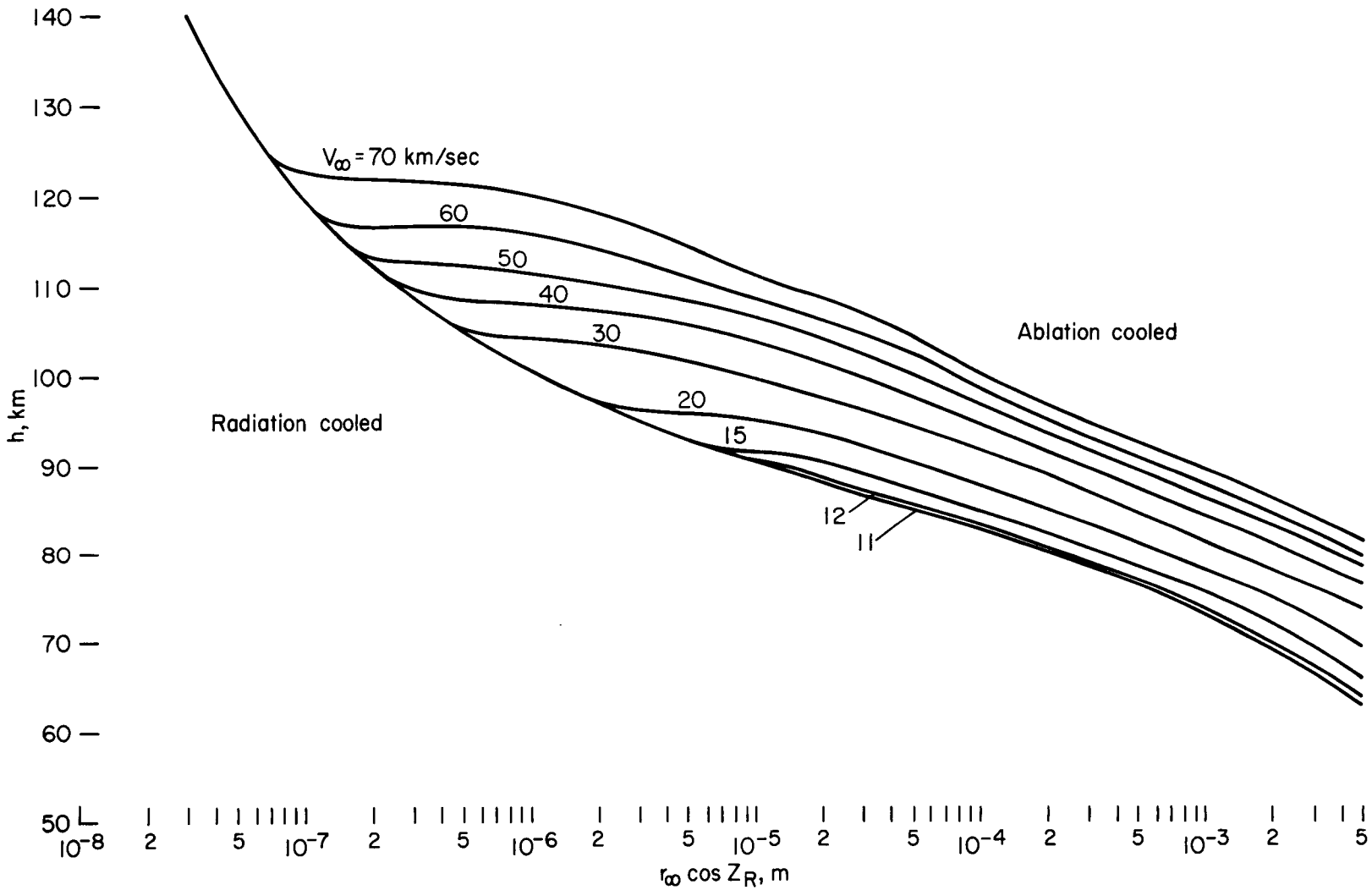

Figure 15.- Altitude at maximum luminous intensity for stone.

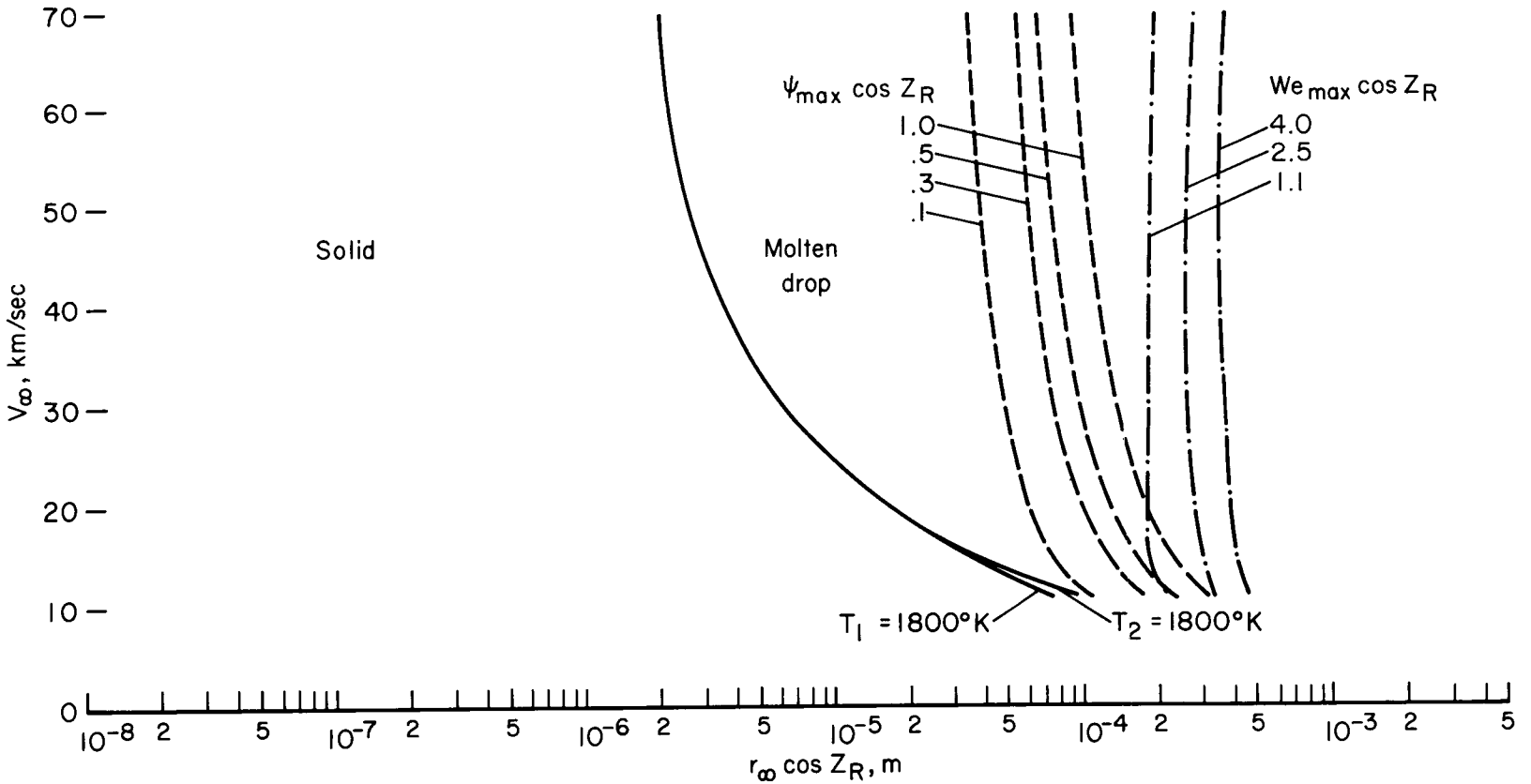

Figure 16.- Limits of validity of analysis for stone.

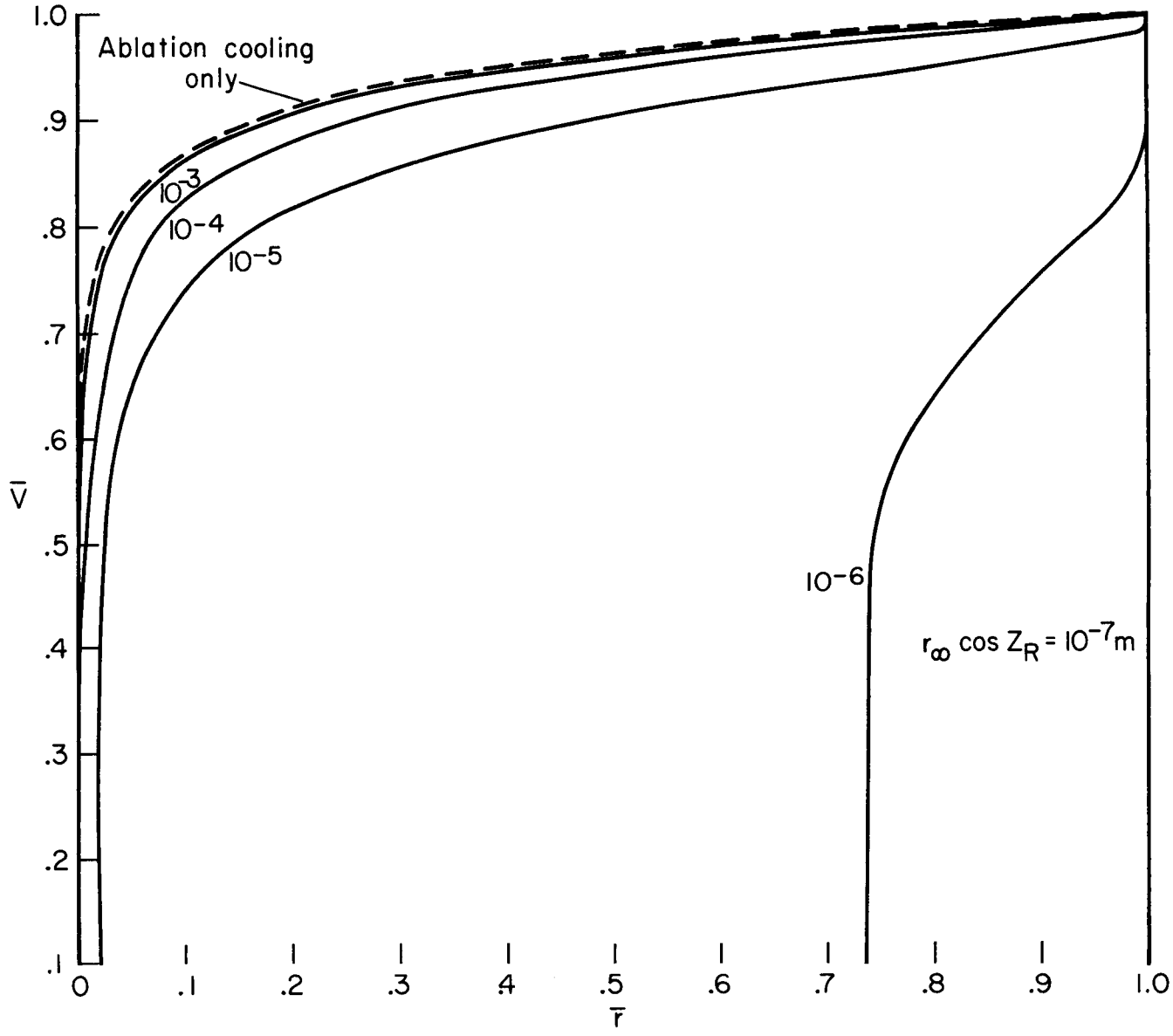

Figure 17.- Plot of $\bar{V}$ vs $\bar{r}$ for stone at V_∞ = 30 km/sec.

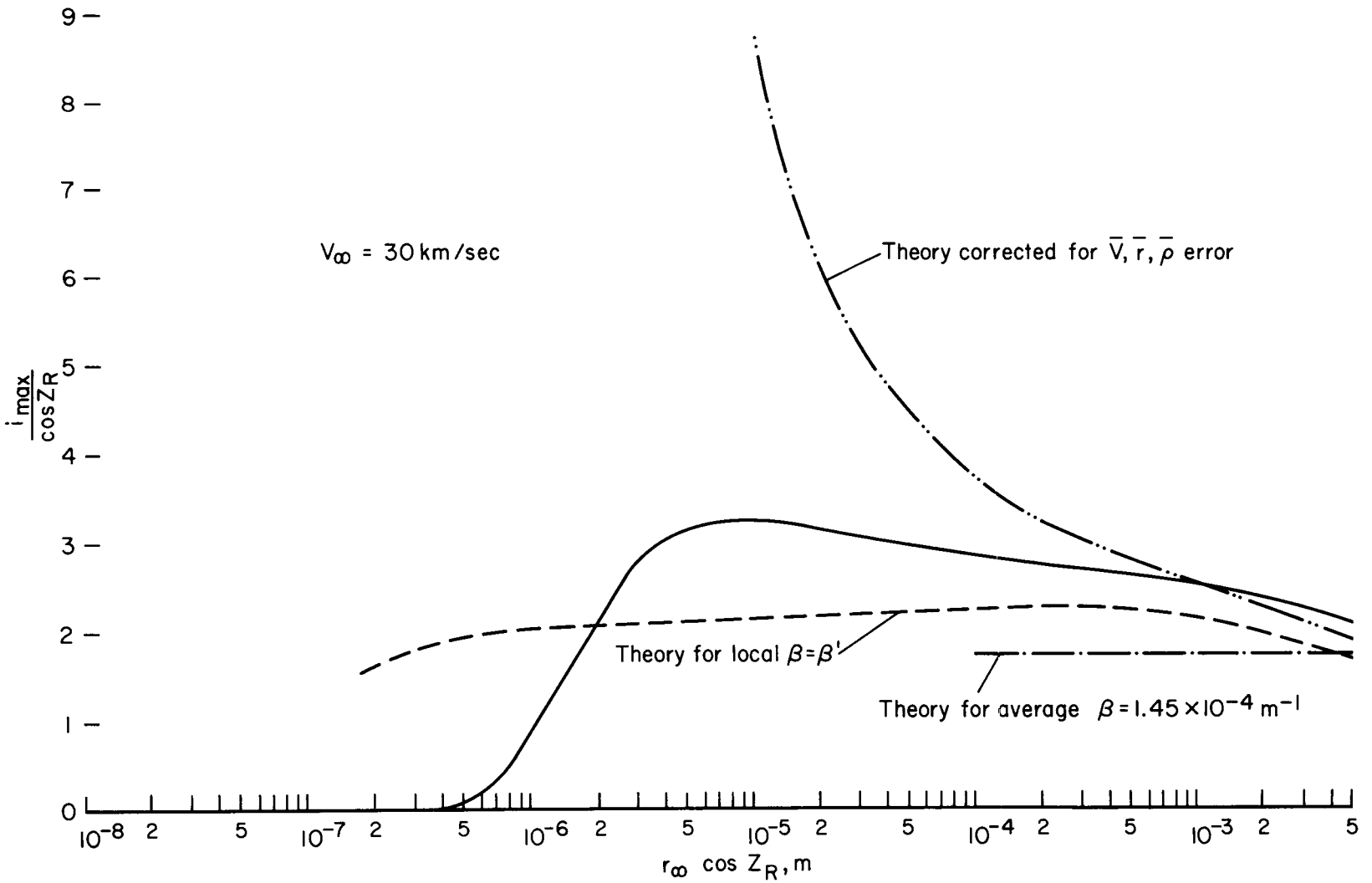

Figure 18.- Maximum luminous intensity coefficient for stone at 30 km/sec.

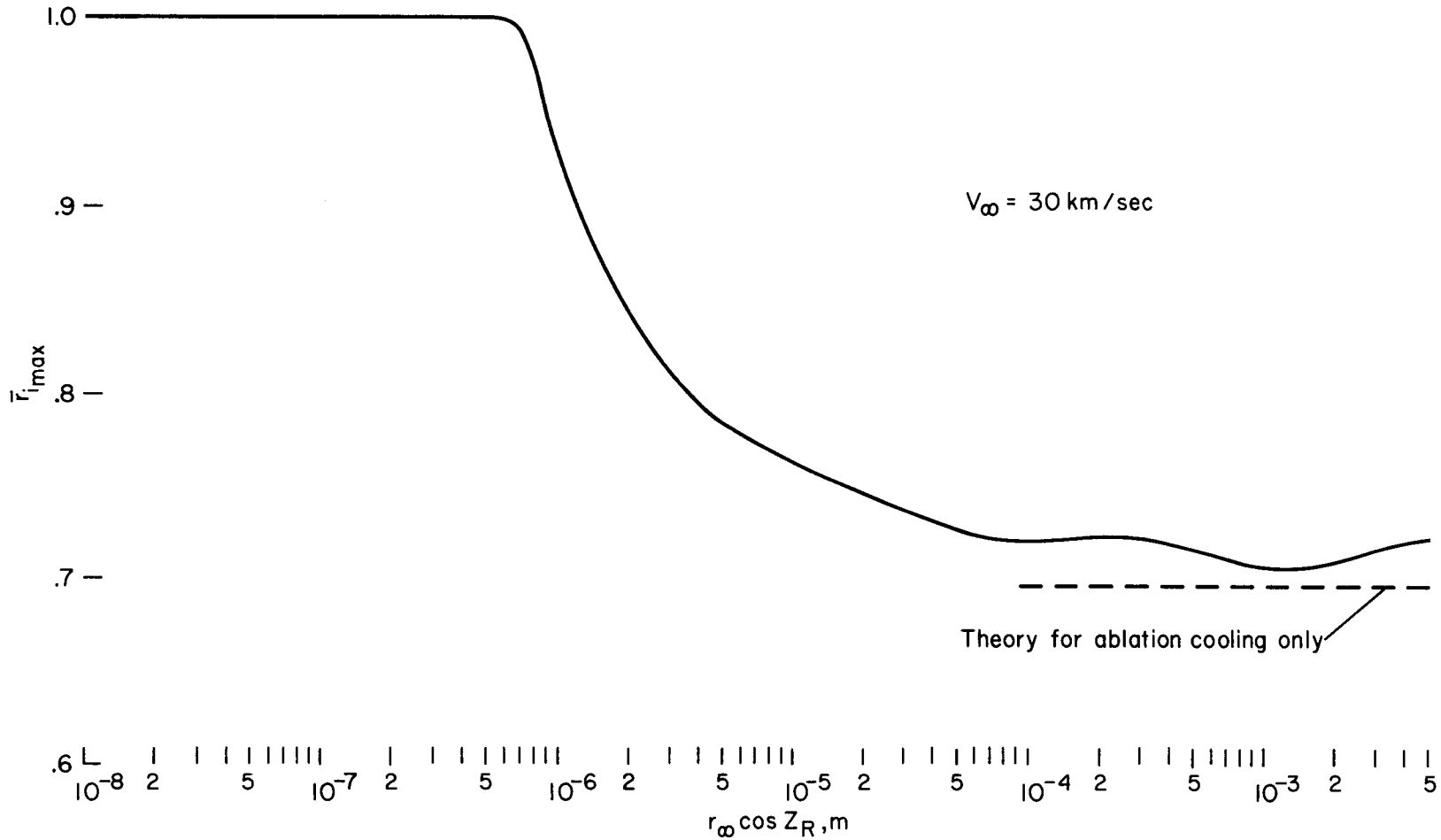

Figure 19.- Values of $\bar{r}$ at maximum luminous intensity for stone at 30 km/sec.

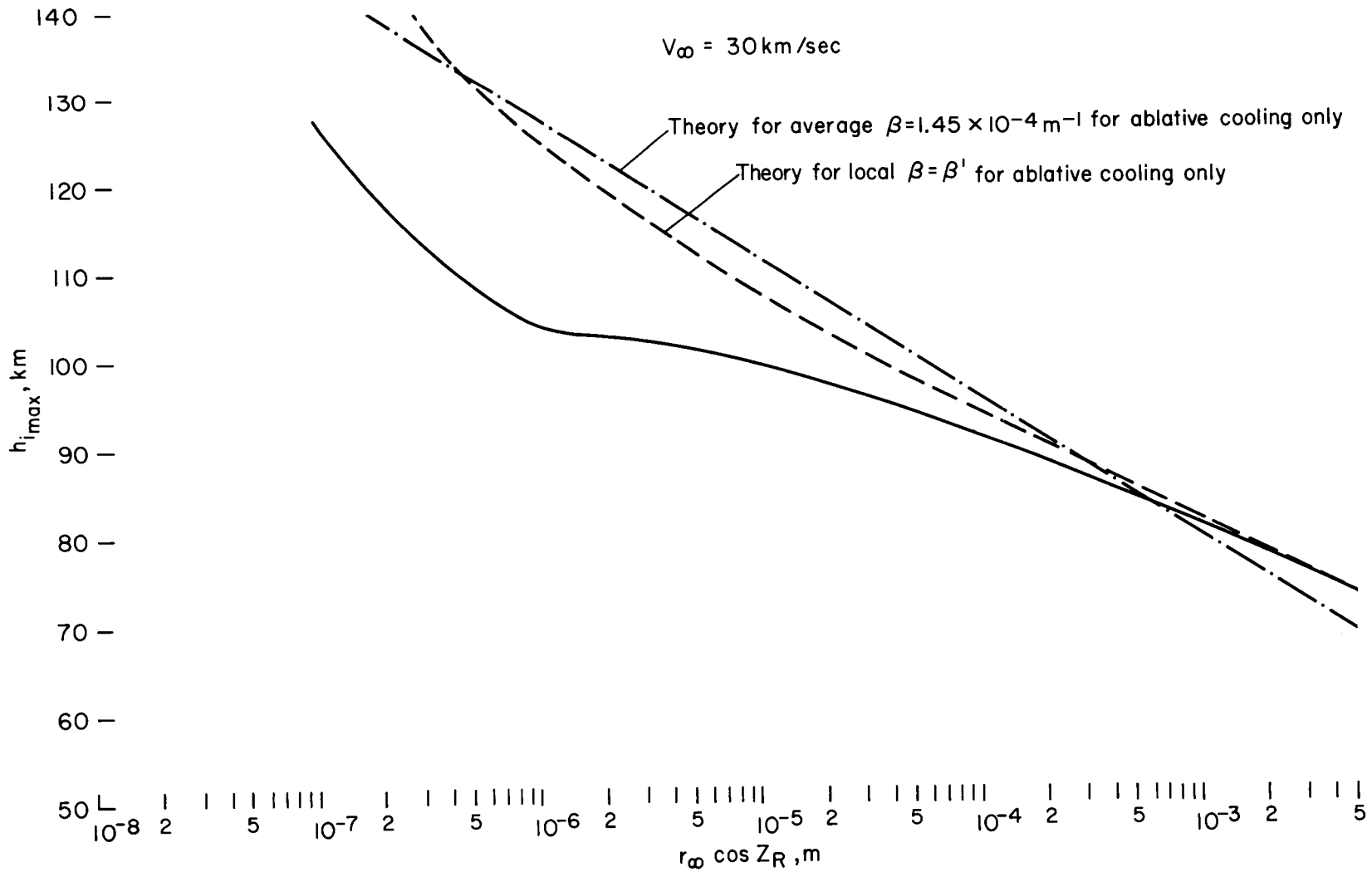

Figure 20.- Altitude at maximum luminous intensity for stone at 30 km/sec.

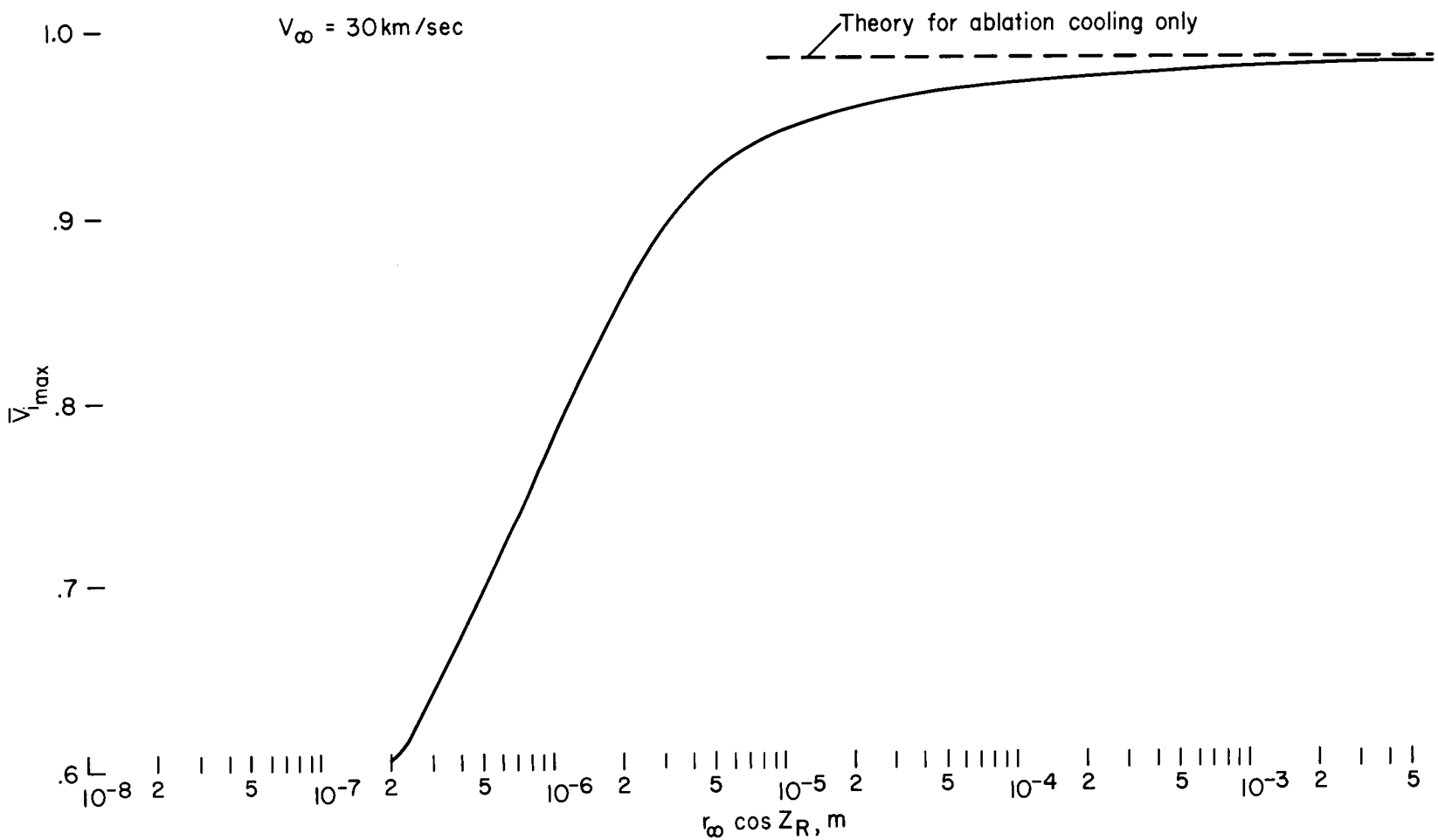

Figure 21.- Values of $\bar{V}$ at maximum luminous intensity for stone at 30 km/sec.

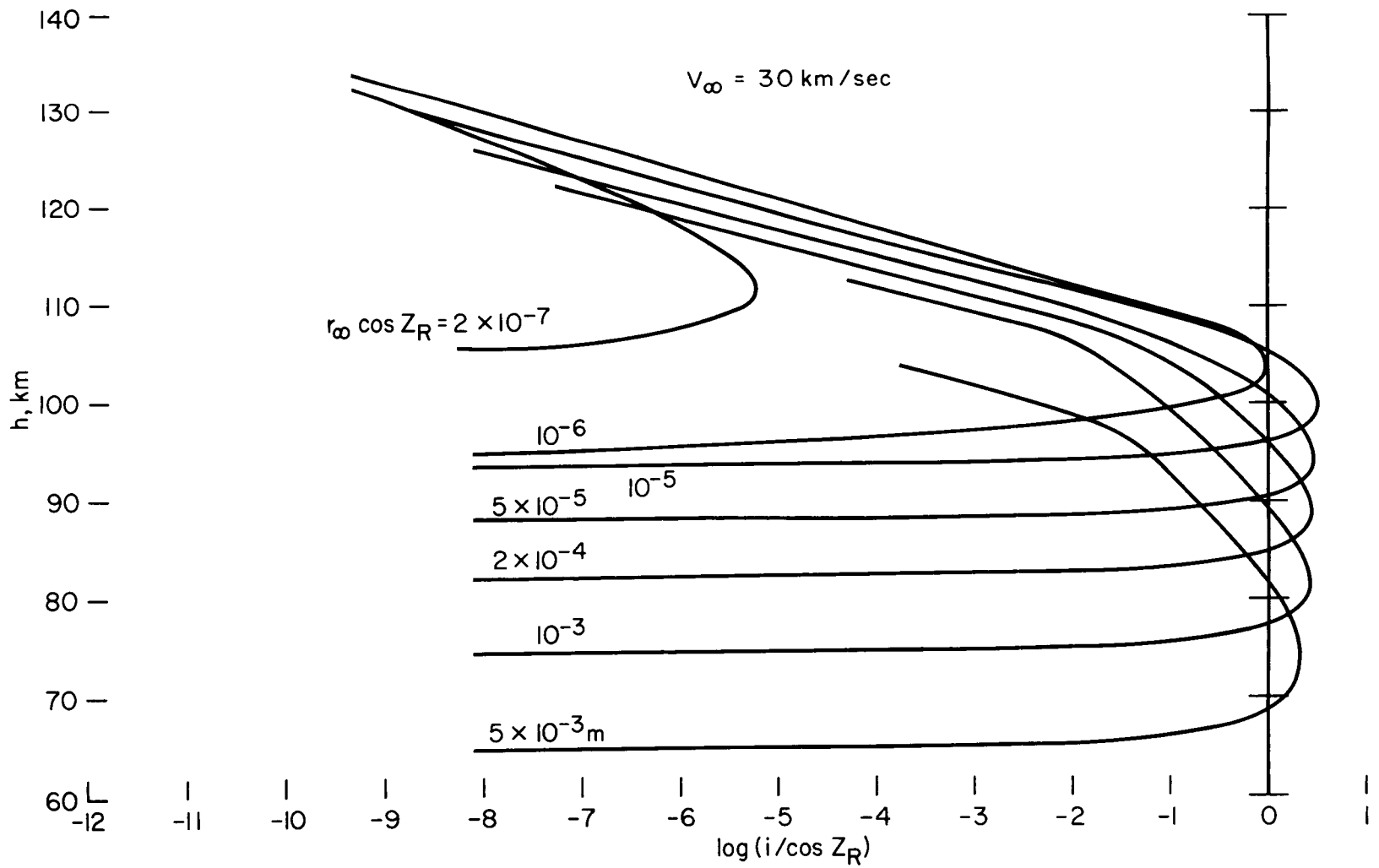

Figure 22.- Values of $\log(i/\cos Z_R)$ versus altitude for stone at 30 km/sec.

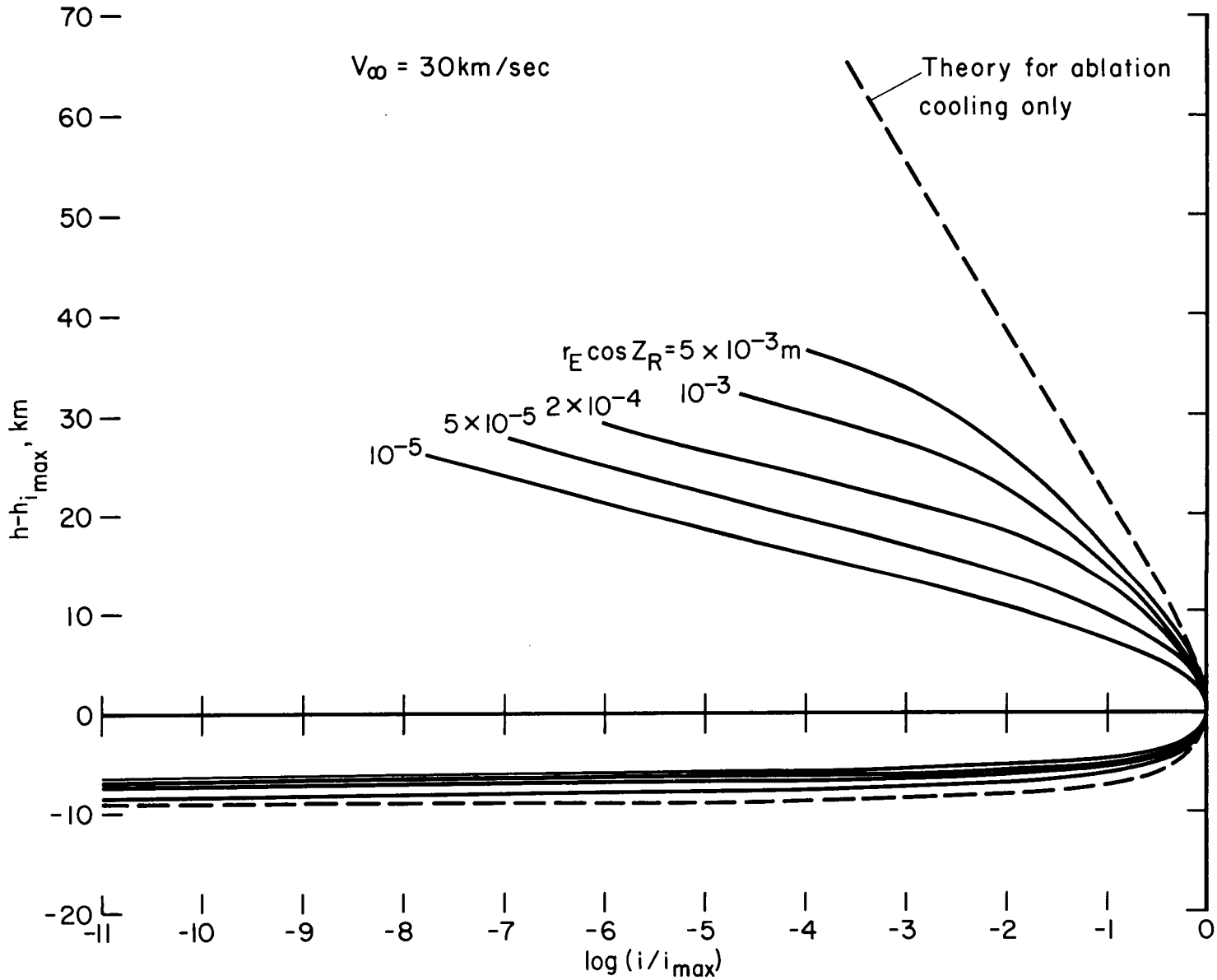

Figure 23.- Normalized plot of $\log(i/i_{max})$ for stone at 30 km/sec.

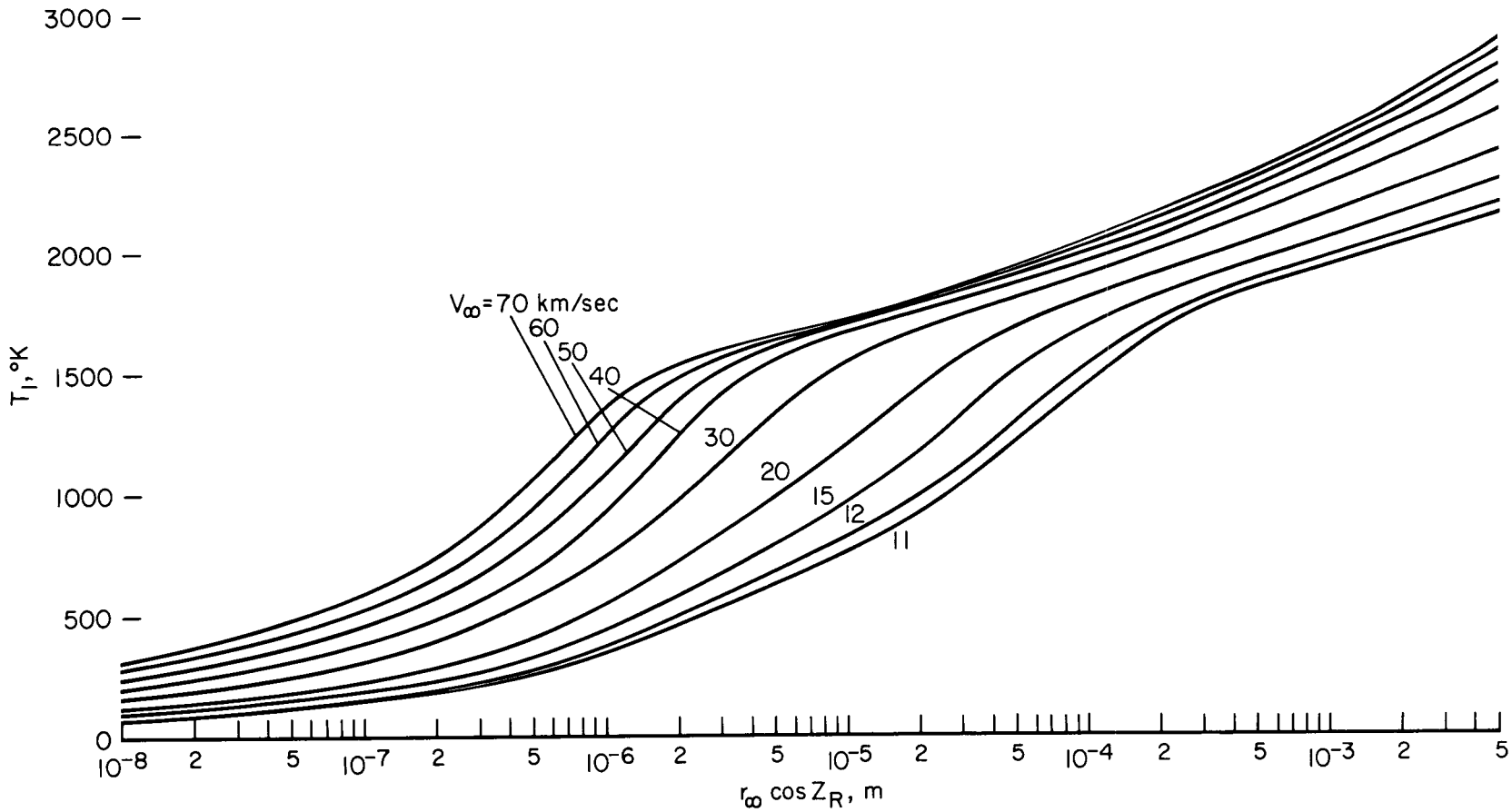

Figure 24.- Front face peak temperature, T_1, for pumice.

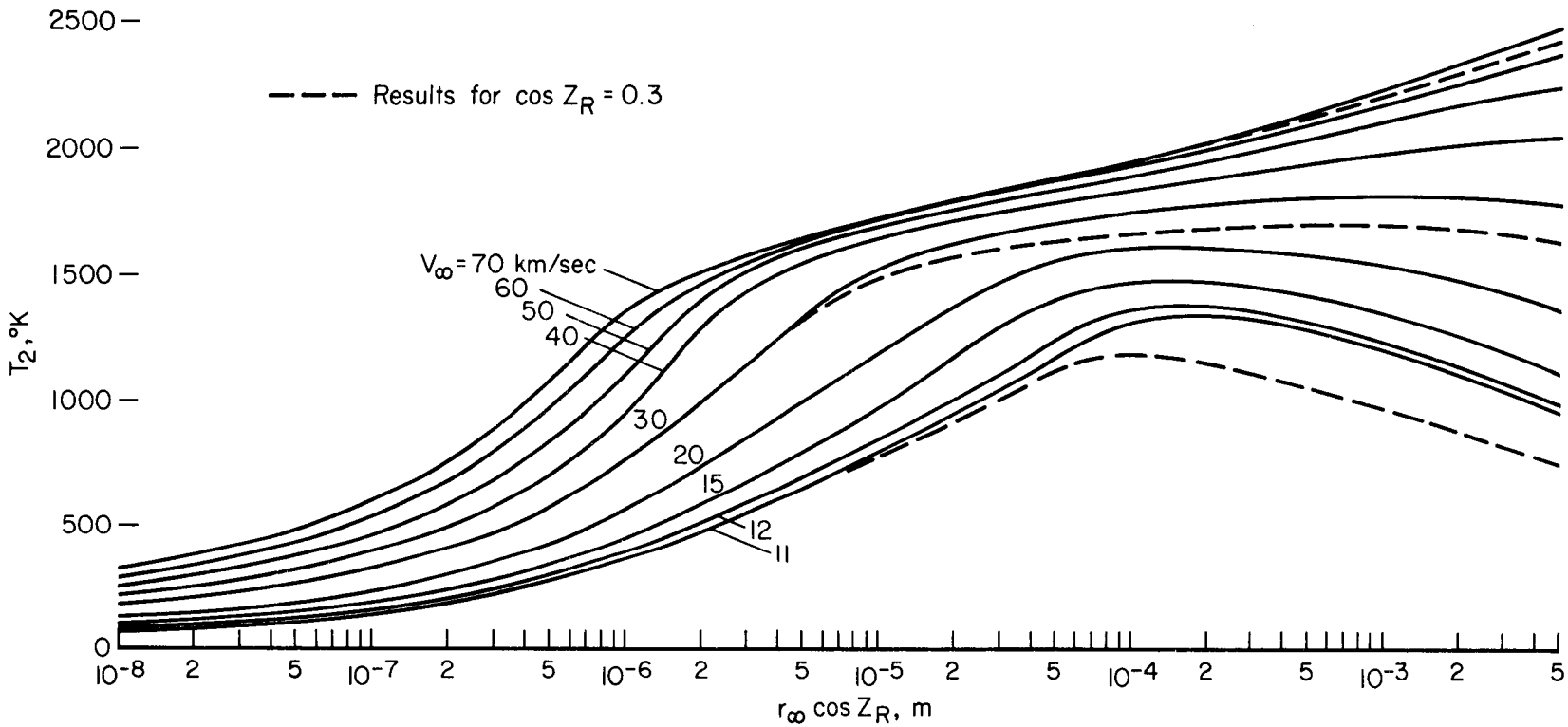

Figure 25.- Rear face peak temperature, T_2, for pumice.

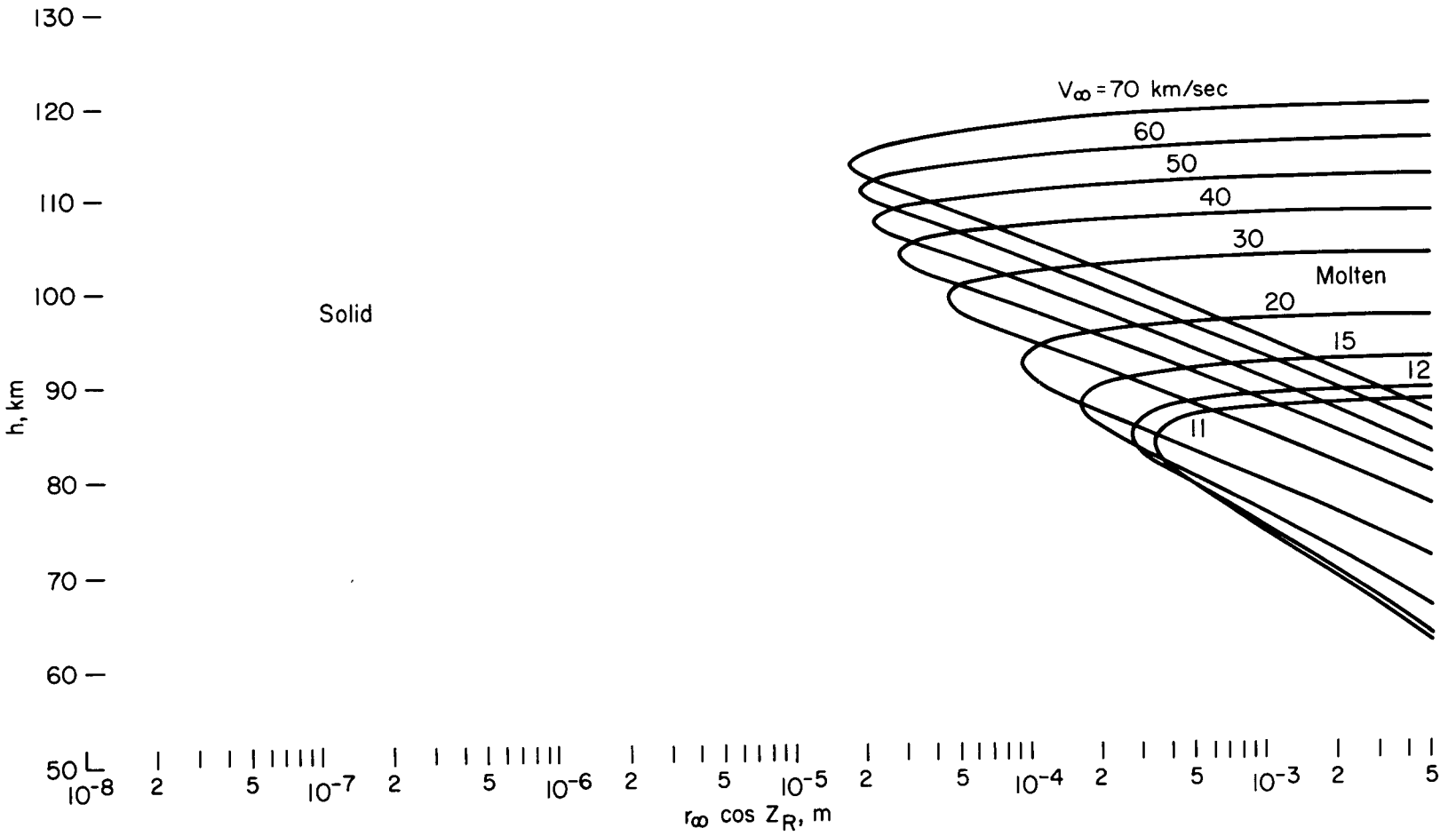

Figure 26.- Front face melting zone for pumice

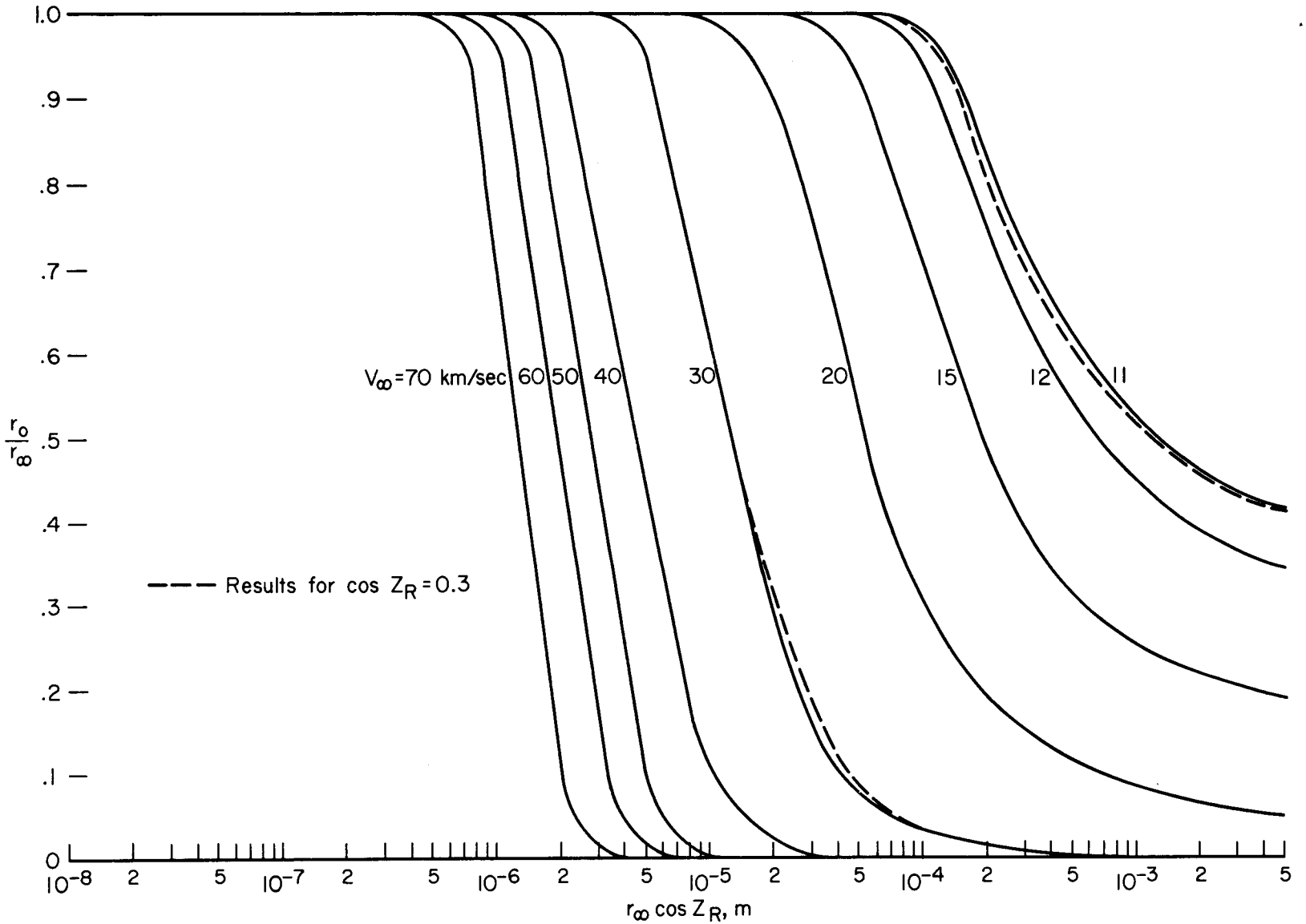

Figure 27.- Ratio of final to entry radius, r_o/r_∞, for pumice.

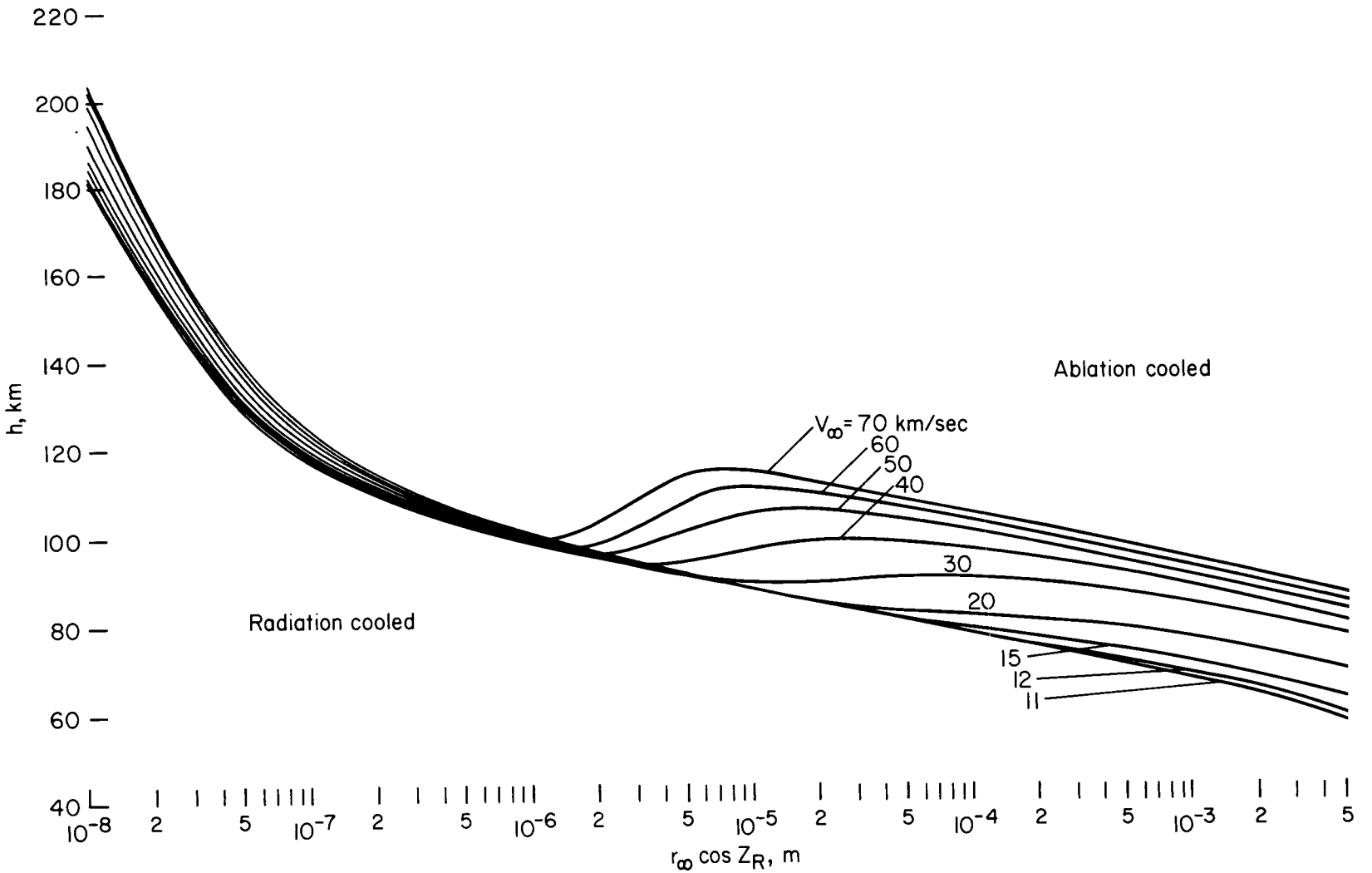

Figure 28.- Final altitude (V = 500 m/sec) for pumice.

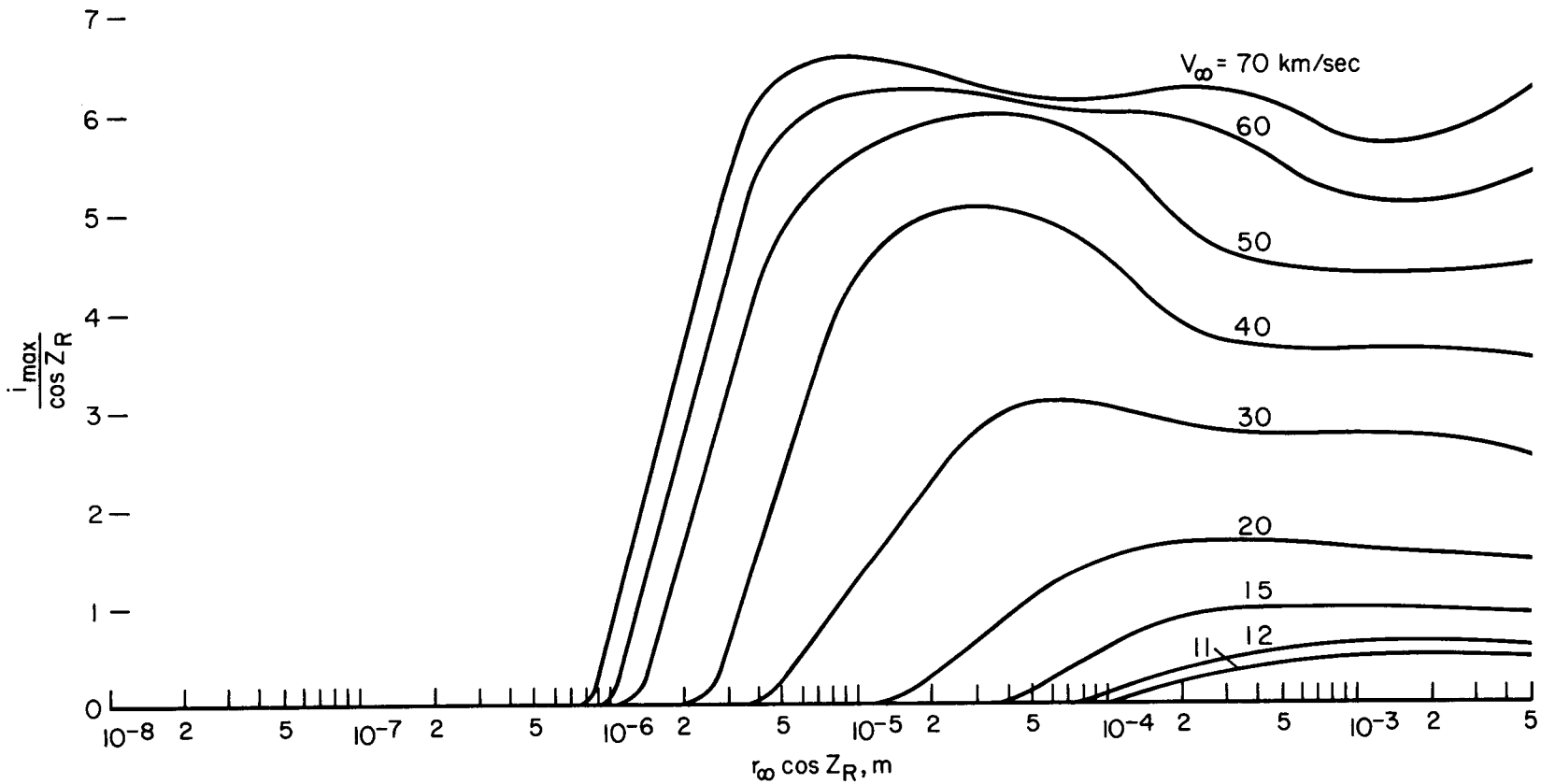

Figure 29.- Maximum luminous intensity coefficient for pumice.

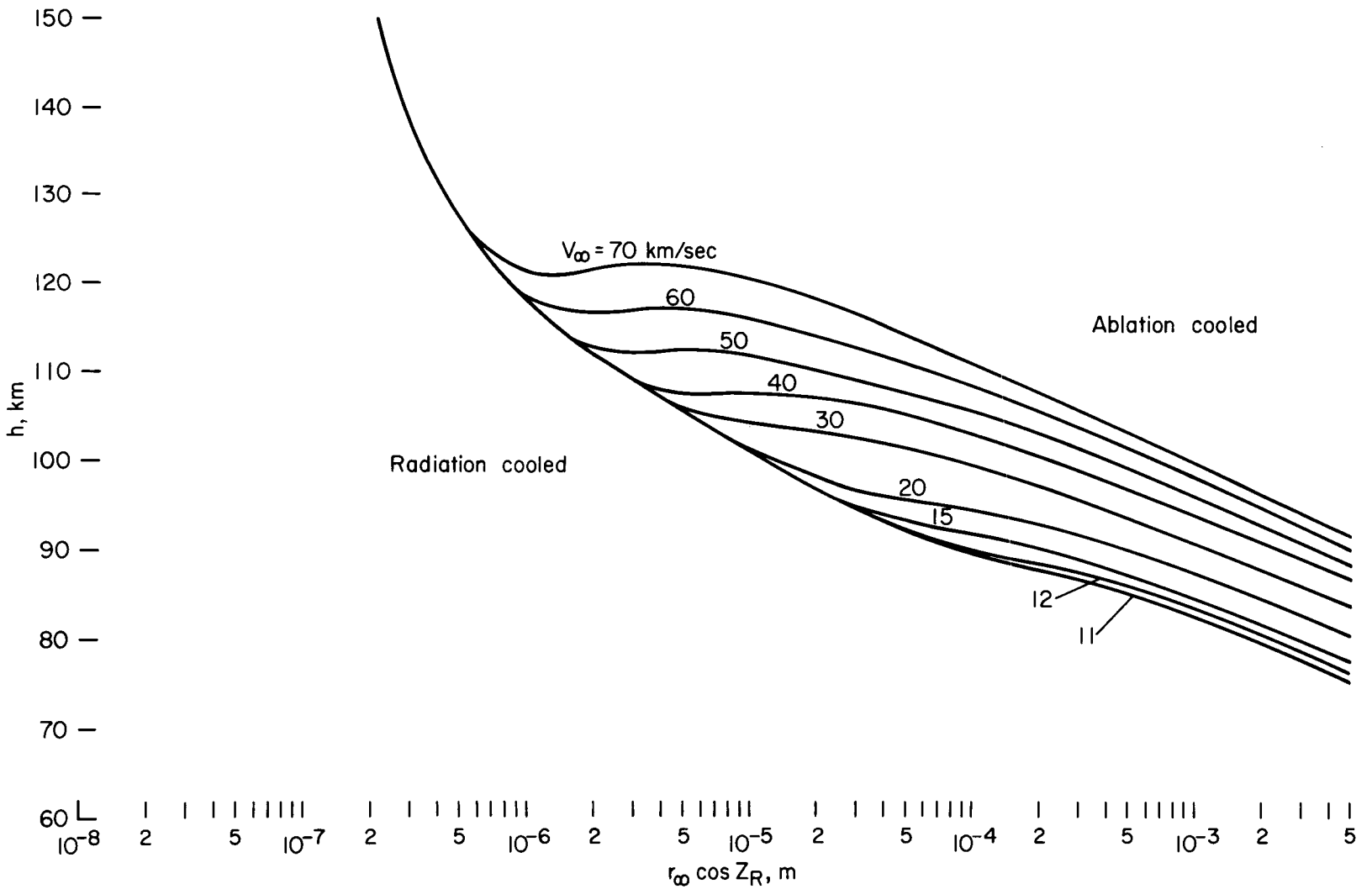

Figure 30.- Altitude at maximum luminous intensity for pumice.

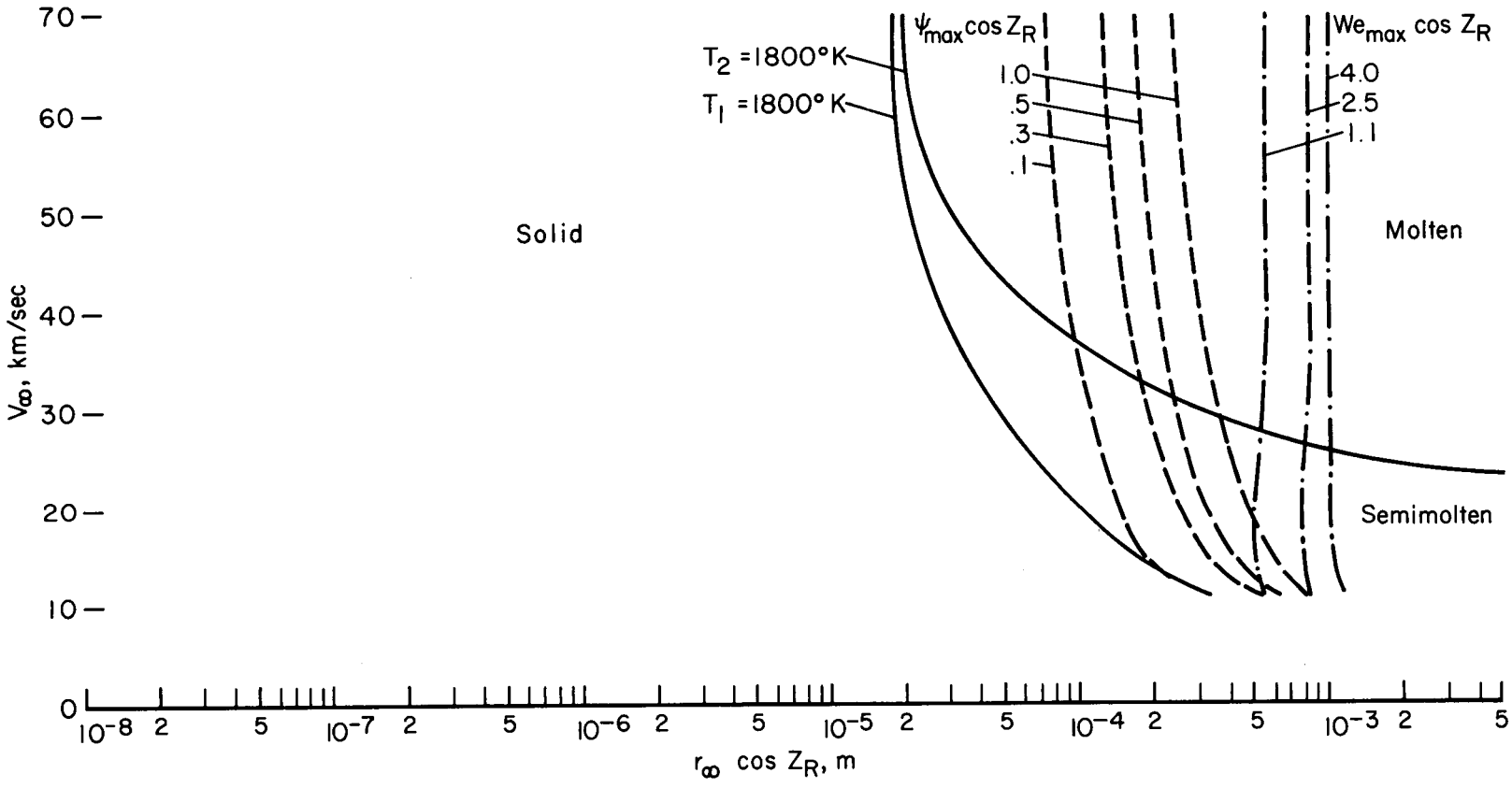

Figure 31.- Limits of validity of analysis for pumice.

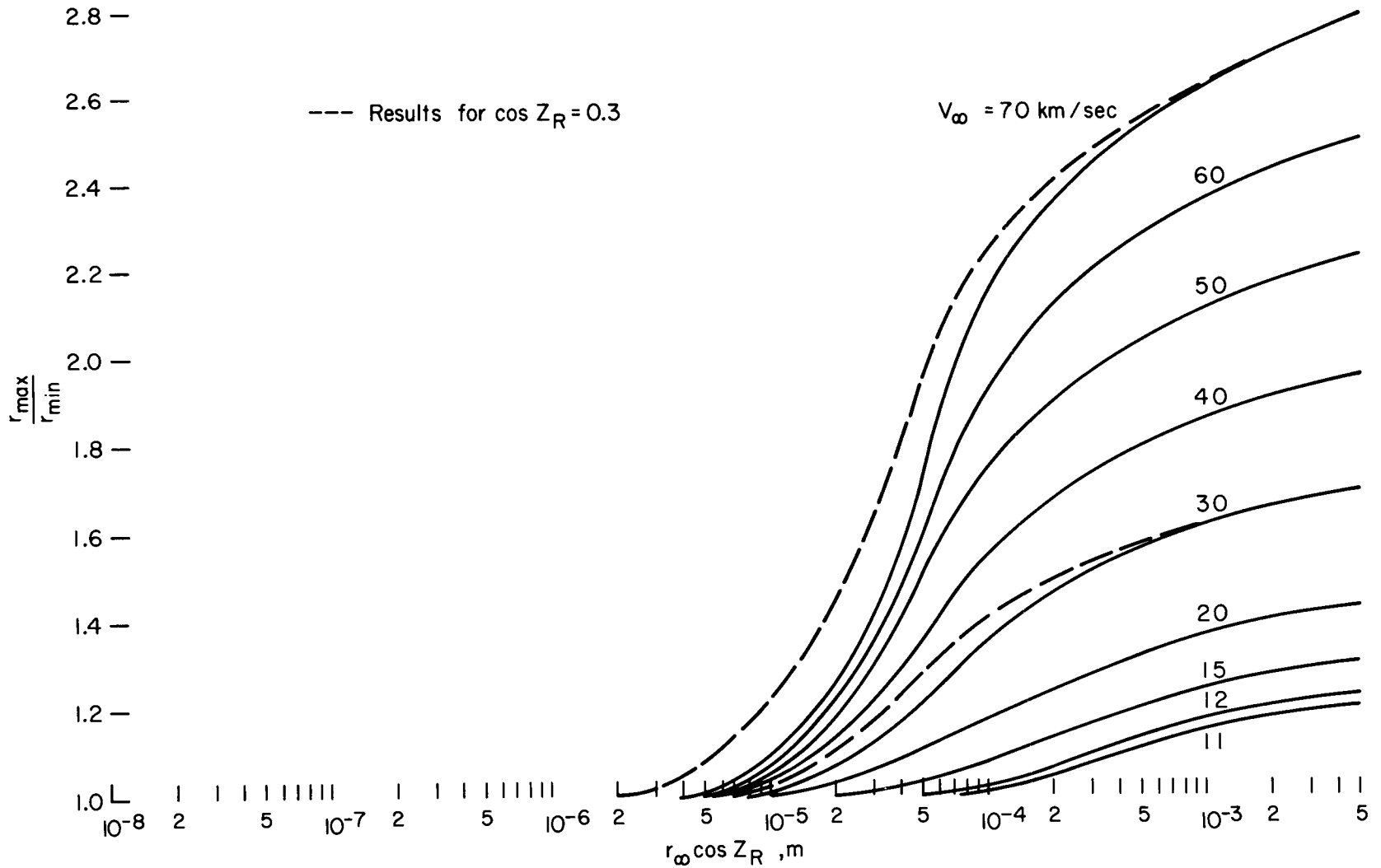

Figure 32.- Ratio of maximum to minimum drag coefficient for pumice.

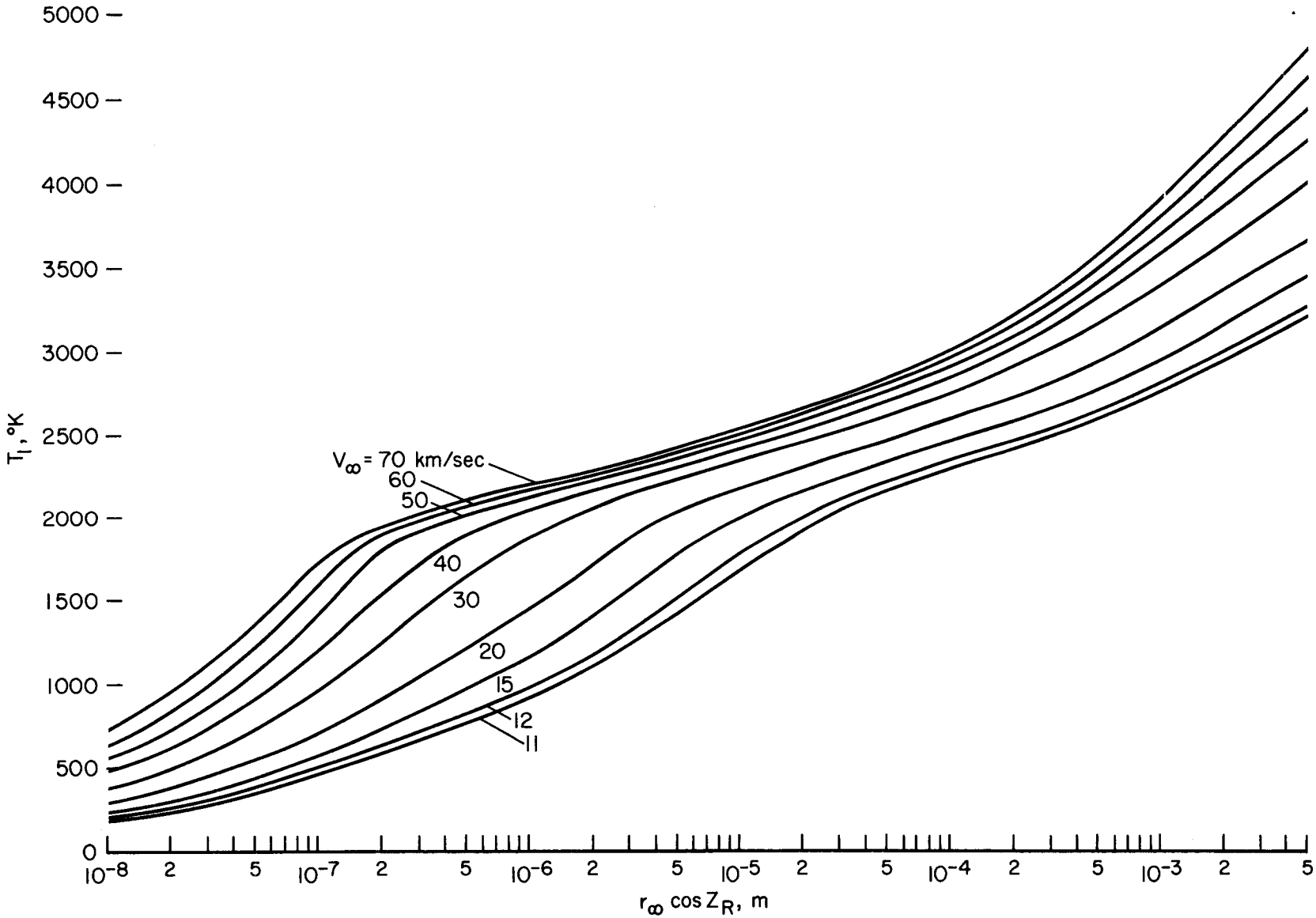

Figure 33.- Front face peak temperature, T_1, for iron.

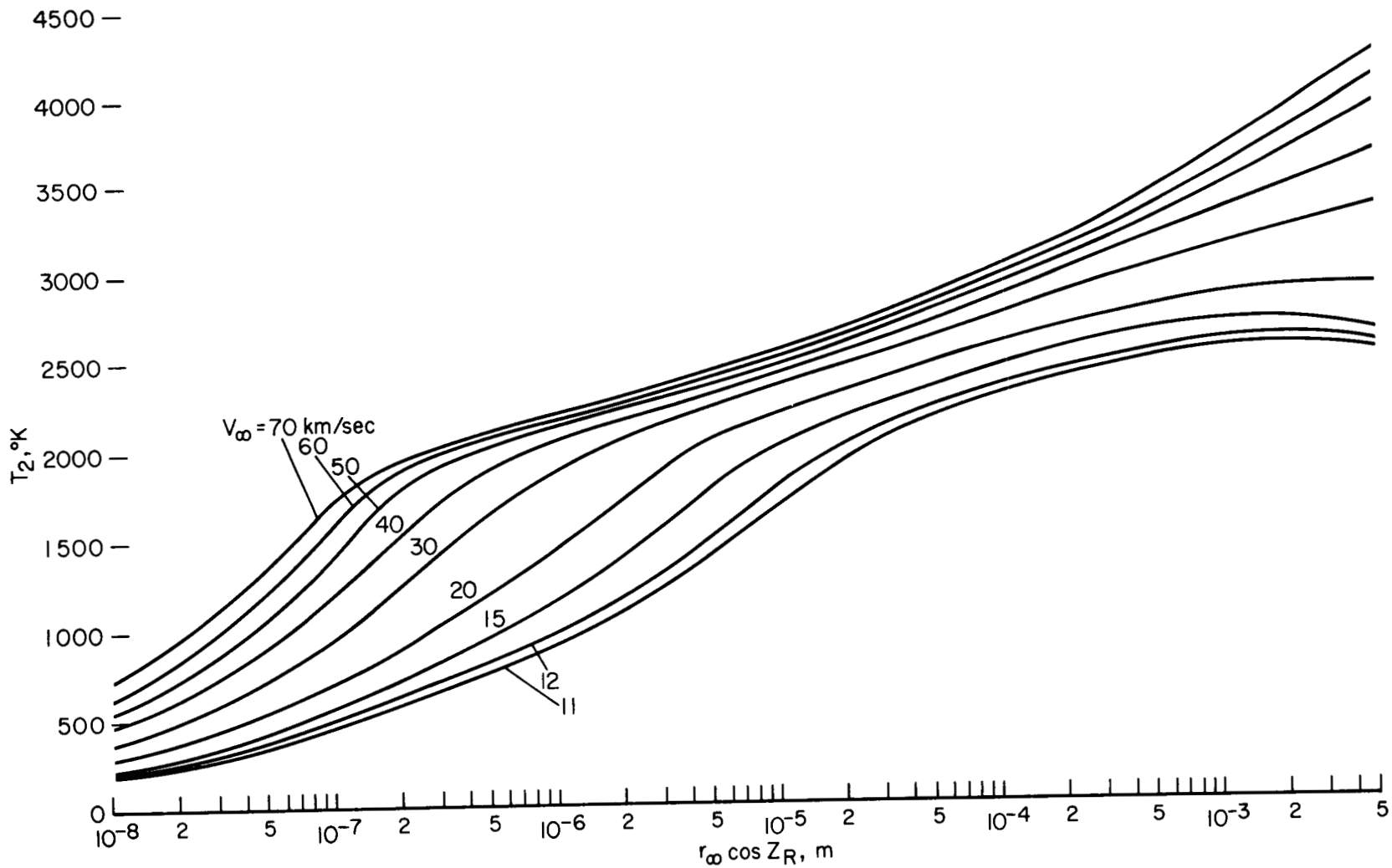

Figure 34.- Rear face peak temperature, T_2, for iron.

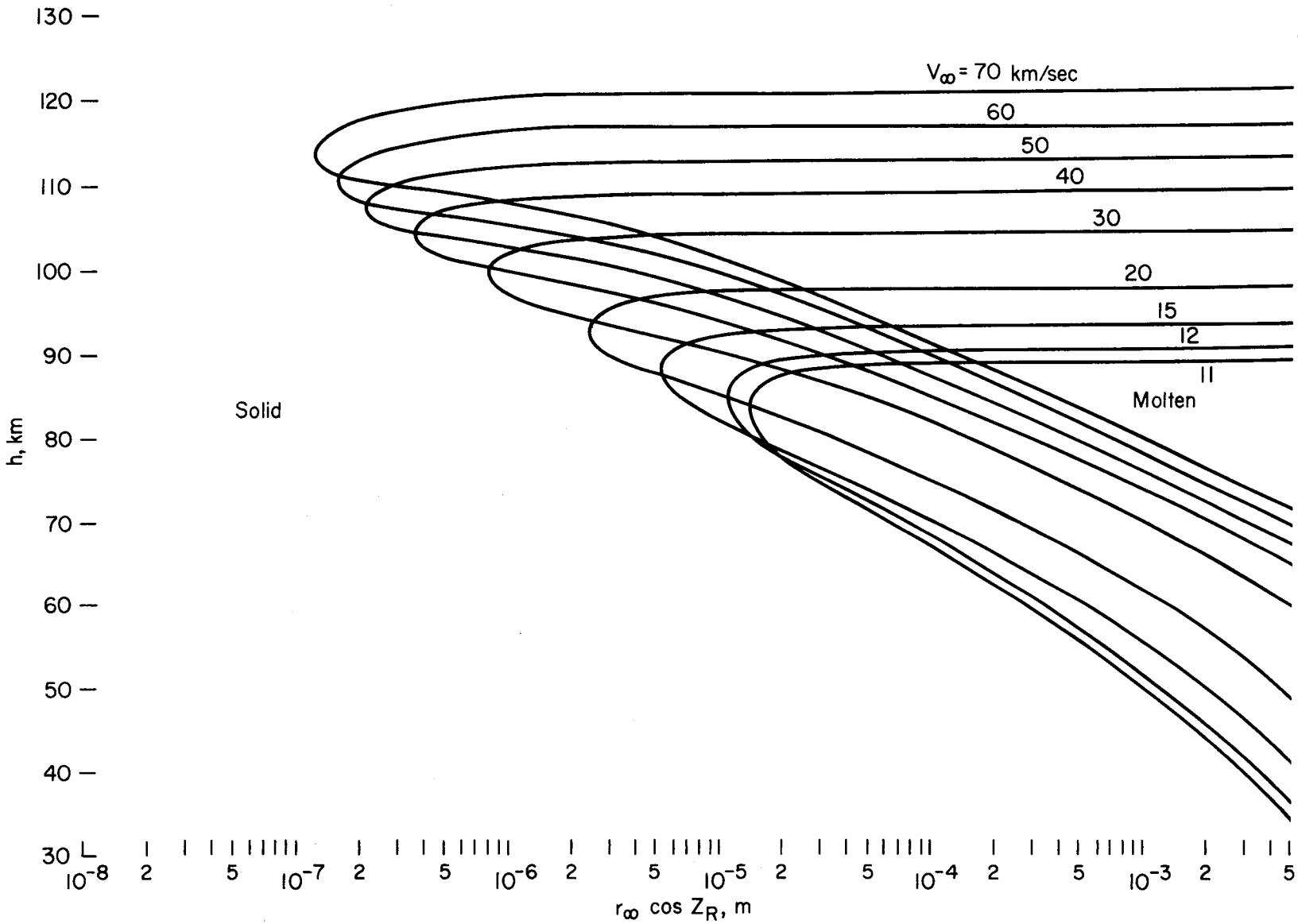

Figure 35.- Front face melting zone for iron.

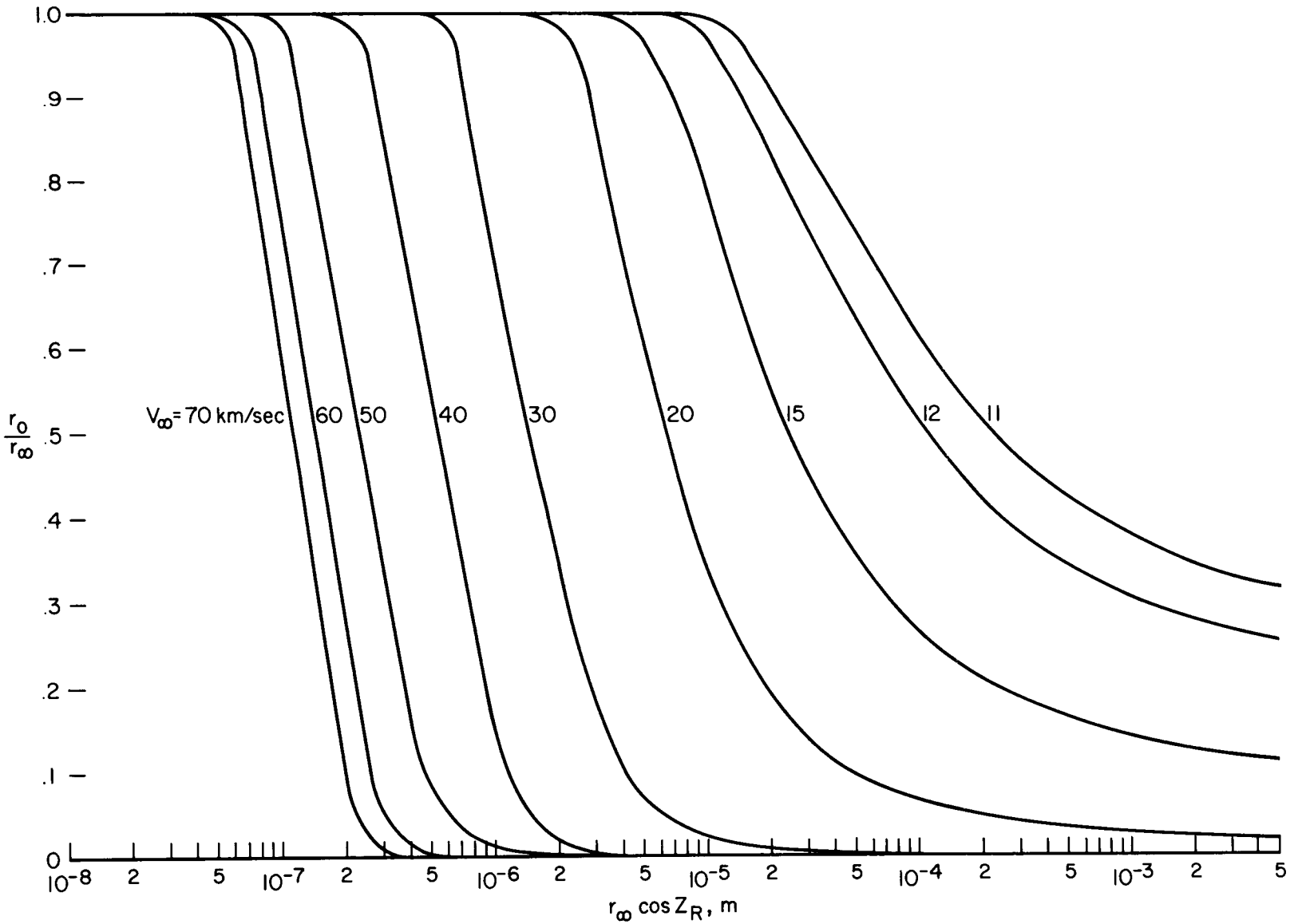

Figure 36.- Ratio of final to entry radius for iron.

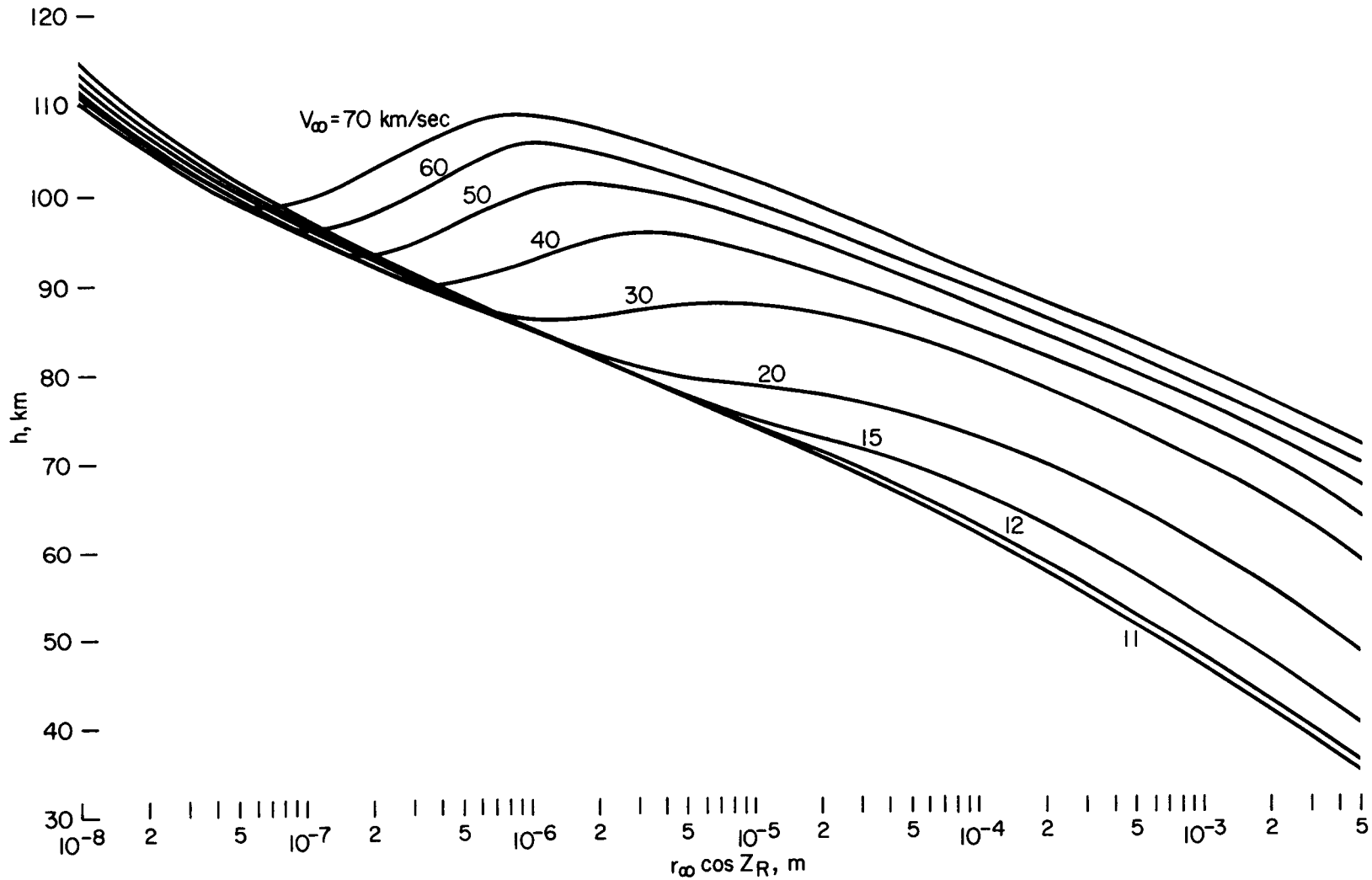

Figure 37.- Final altitude (V = 500 m/sec) for iron.

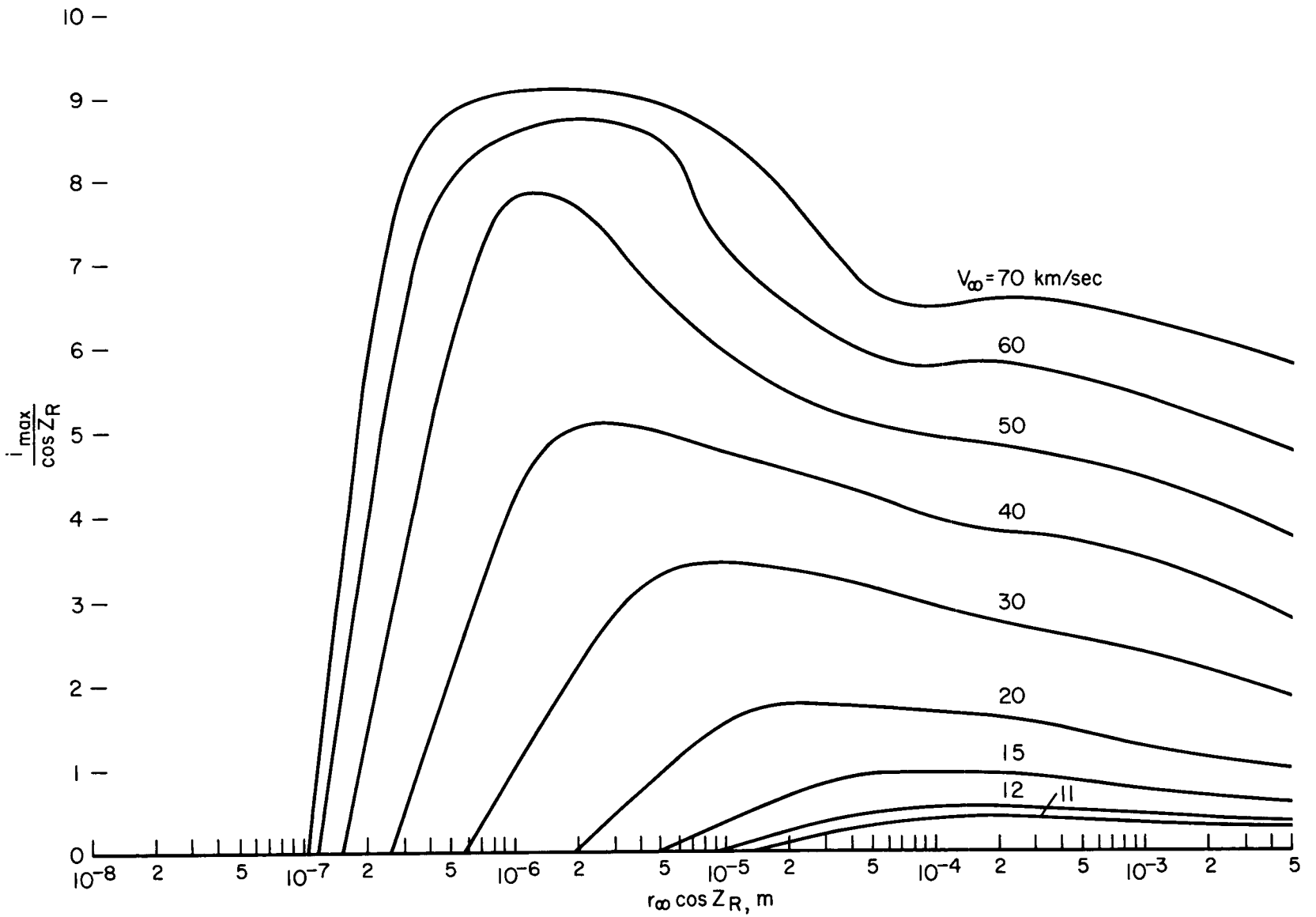

Figure 38.- Maximum luminous intensity coefficient for iron.

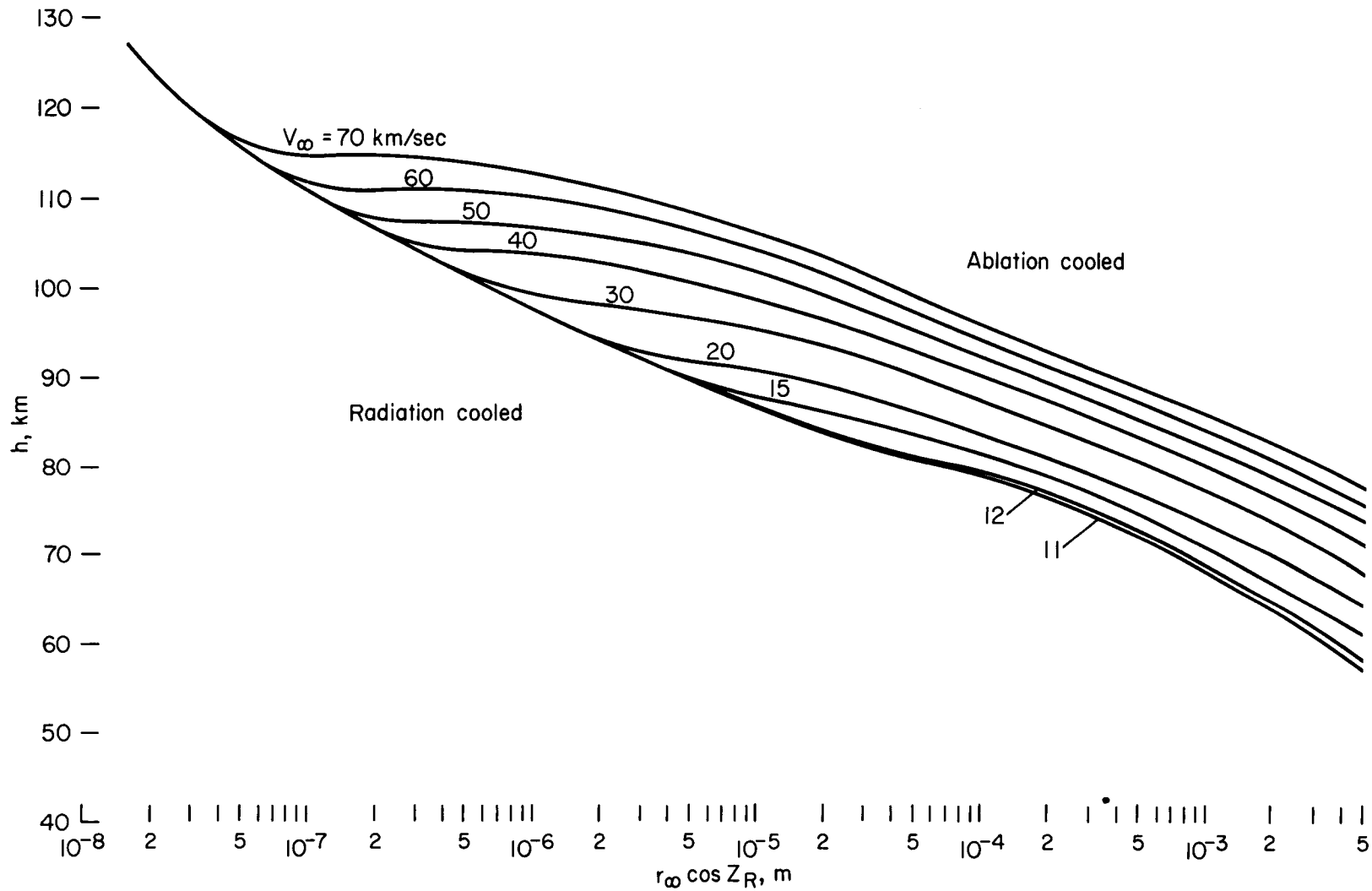

Figure 39.- Altitude at maximum luminous intensity for iron.

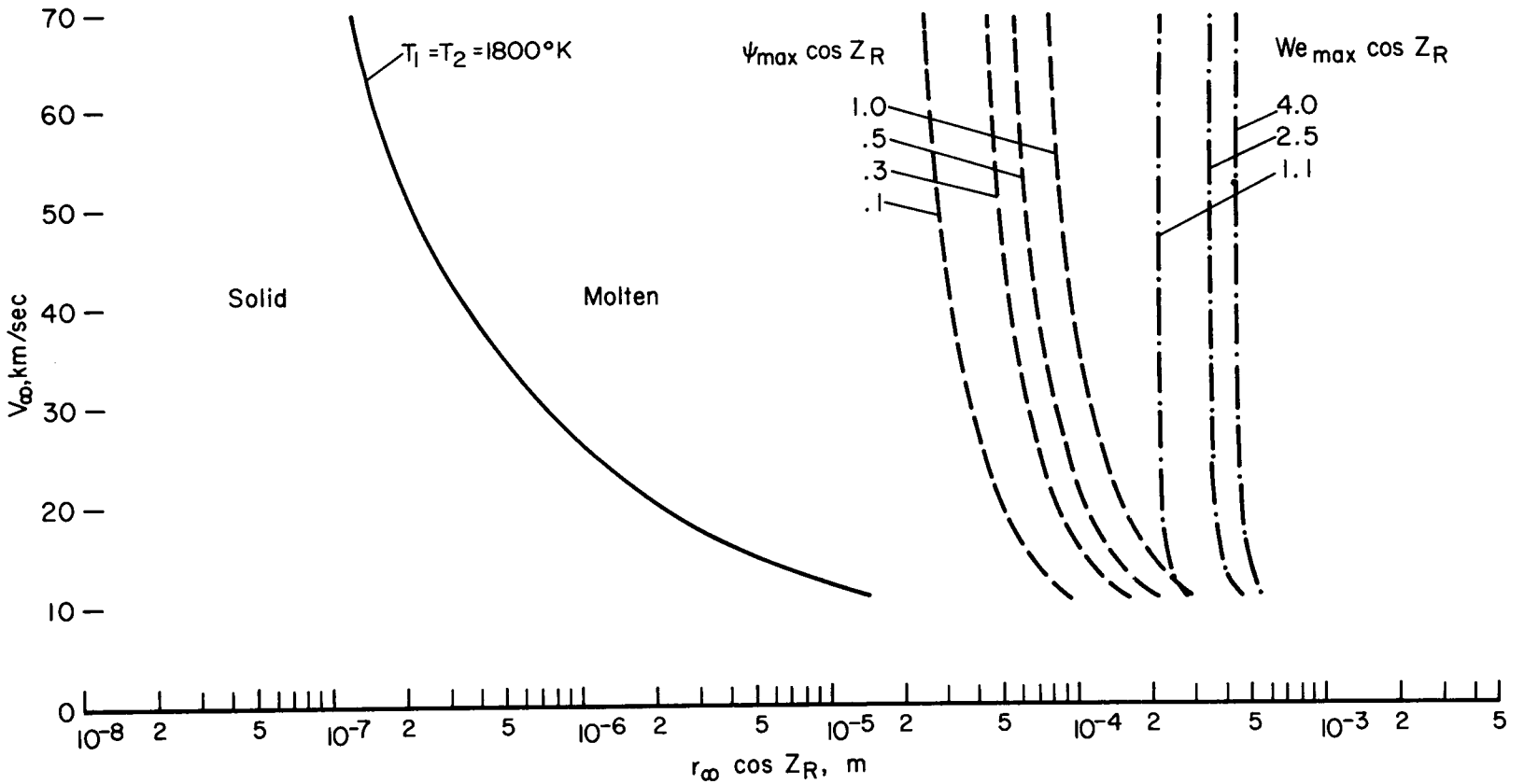

Figure 40.- Limits of validity of analysis for iron.

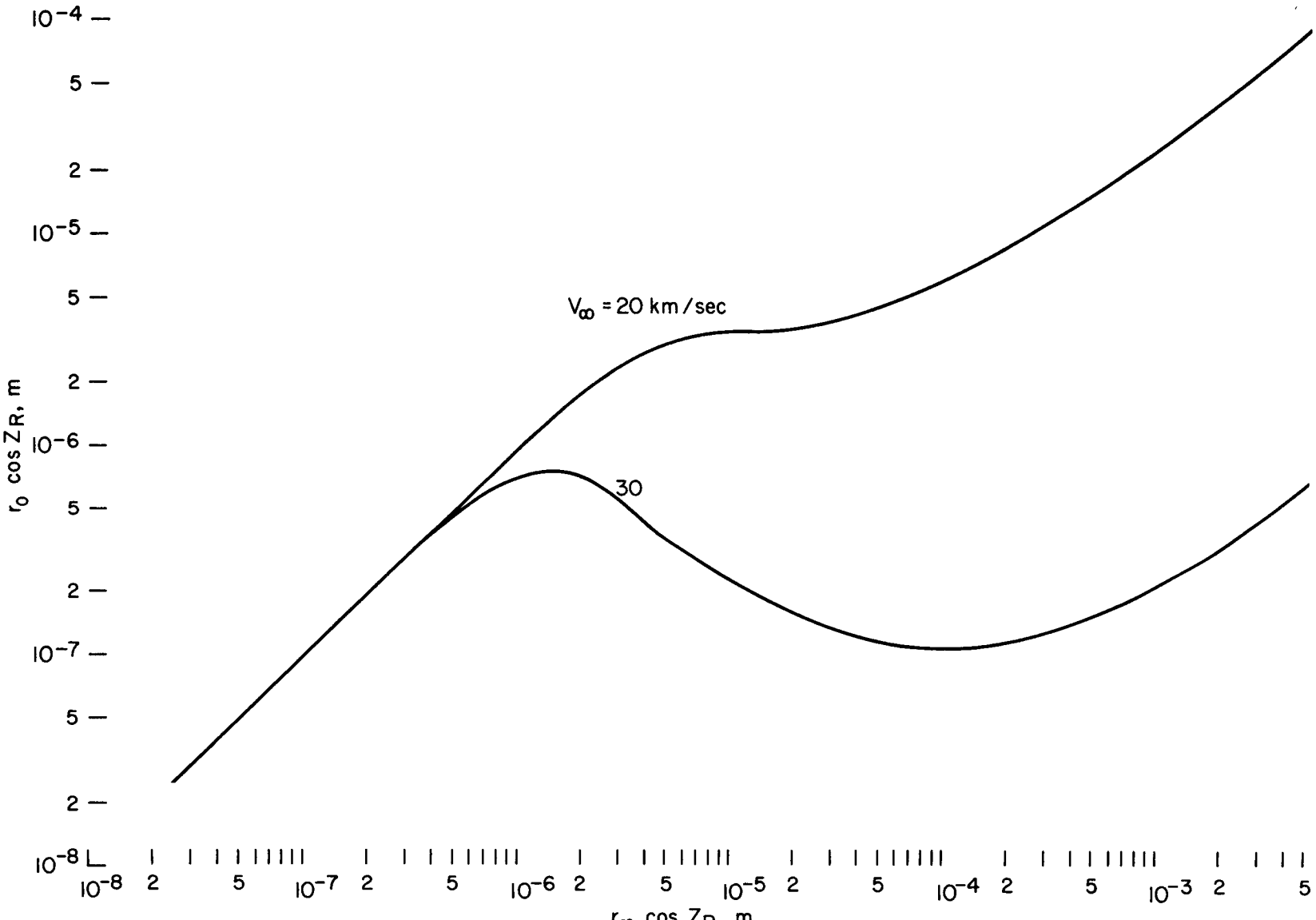

Figure 41.- Final size for iron.

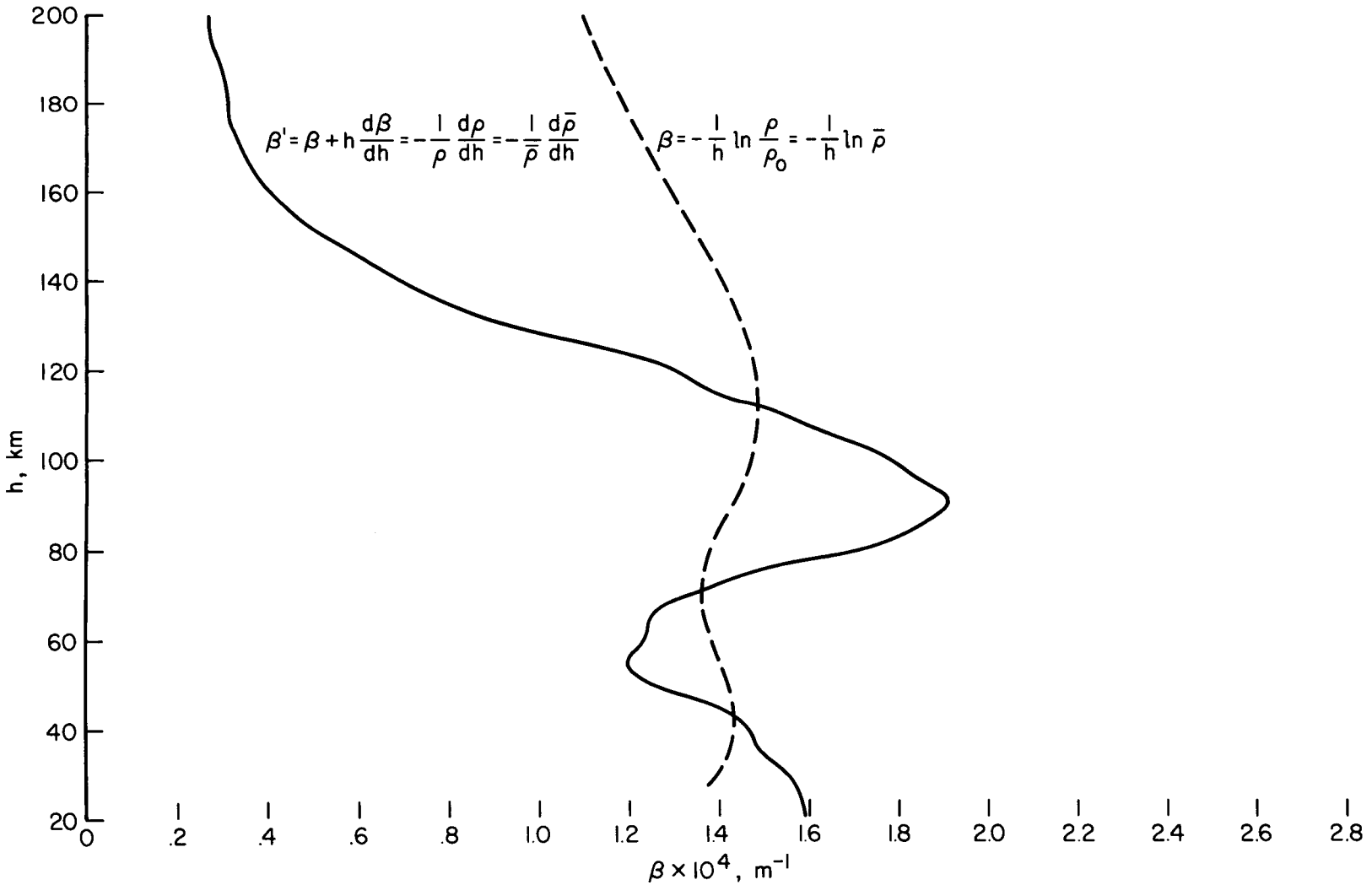

Figure 42.- Variation of inverse scale height with altitude.

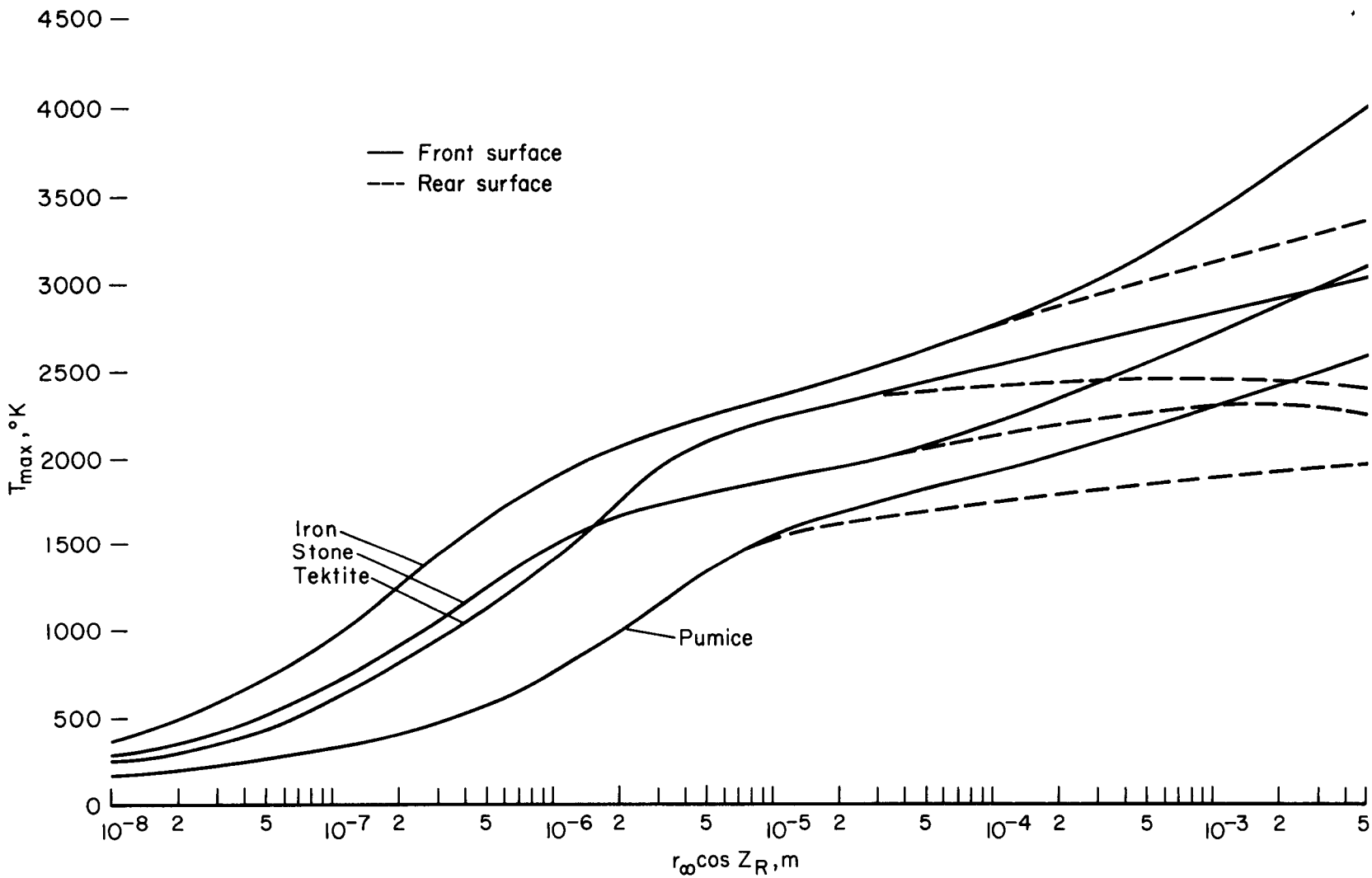

Figure 43.- Comparison of front and rear surface maximum temperatures at 30 km/sec.

NASA-Langley, 1965 A-1076